Article
Vol. 23, No. 3, p. 439–460, June 2019
https://doi.org/10.1007/s12303-018-0044-x
pISSN 1226-4806 eISSN 1598-7477
Geosciences Journal GJ

Tsunami hazard from submarine landslides: scenario-based assessment in the Ulleung Basin, East Sea (Japan Sea)

Roger Urgeles[1], Jang-Jun Bahk[2]*, Sang-Hoon Lee[3], Senay Horozal[4], Deniz Cukur[4], Seong-Pil Kim[4], Gil-Young Kim[4], Sueng-Won Jeong[5], and In-Kwon Um[4]

[1]Departament de Geociències Marines, Institut de Ciències del Mar (CSIC), Pg. Marítim de la Barceloneta, 37-49, 08003 Barcelona, Spain
[2]Department of Oceanography and Ocean Environmental Sciences, Chungnam National University, Daejeon 34134, Republic of Korea
[3]Marine Geology & Geophysics Laboratory, Korea Institute of Ocean Science and Technology, Busan 49111, Republic of Korea
[4]Petroleum and Marine Research Division, Korea Institute of Geoscience and Mineral Resources, Daejeon 34132, Republic of Korea
[5]Geologic Environment Research Division, Korea Institute of Geoscience and Mineral Resources, Daejeon 34132, Republic of Korea

ABSTRACT: In this study we use a scenario-based approach to highlight potential tsunami hazard from actual Late Pleistocene submarine landslides in the Ulleung Basin: two submarine landslides on the western slope of the Ulleung Basin, north and south of the Hupo Bank (2.53 and 1.12 km^3 respectively) and a landslide (15.1 km^3) on the continental slope south of the Ulleung Basin. The simulations attempt to highlight the consequences, should one of these events occur at Present. Results of the simulations indicate potential local hazard zones with very local waves < 2 m high in the Korean coast of the East Sea that could result from mid-sized landslides, not exceeding 3 km^3 on the western slope of the basin. Time available for early warning since onset of these events is between 15–30 minutes. On the other hand, the continental margin south of the Ulleung Basin is an area where landslide tsunamis with significant hazard potential could originate. New landslides of similar size to those of the Late Pleistocene could produce tsunami waves > 3 m in the stretch of coastline from Ulsan in the south to Uljin in the north. The timing available for early warning from landslide tsunamis originating in this area is 15–30 minutes along the affected section of the shoreline. We also suggest a Probabilistic Tsunami Hazard Assessment (PTHA) for comprehensive assessments of the Korean coast of the East Sea. PTHA accounts for uncertainties in location, release mechanisms, evolution, and return periods of submarine landslides as well as epistemic uncertainty. However, to constrain these uncertainties detailed information on source areas, recurrence period and dynamics of submarine landslides is necessary and calls for additional data collection and further studies.

Key words: submarine landslides, tsunami hazard, Ulleung Basin, East Sea (Japan Sea)

Manuscript received November 8, 2017; Manuscript accepted July 20, 2018

1. INTRODUCTION

Tsunamis threaten coastal communities, infrastructure, and global economies (Morgan et al., 2009). The destructive power and damaging effects of tsunamis were shown by the catastrophic 2004 Sumatra (Mw 9.3) and 2011 Tohoku (Mw 9.0) earthquakes (e.g., Titov et al., 2005; Mori et al., 2011). Despite most tsunamis originate from subduction earthquakes (Satake and Atwater, 2007; Harbitz et al., 2014), submarine landslides may also generate tsunami (Papadopoulos et al., 2014; ten Brink et al., 2014). In the past, however, tsunamis generated by submarine landslides have been overlooked by the tsunami research community (Gusiakov, 2003; Tinti, 2003; Grilli et al., 2009; Harbitz et al., 2014).

Submarine landslide tsunamis differ from earthquake tsunamis in a number of ways (Fig. 1). Earthquakes make almost instantaneous energy input into the water column over the entire ruptures, but submarine landslides, which travel up to several tens of meters a second, are less efficient in tsunami generation (Tappin, 2017). The maximum wave height and energy of generated surface waves depend on various landslide parameters and factors, including landslide volume, type of landslide (viscous or rigid), landslide density, landslide position (relative height or depth), and slope angle (Fine et al., 2003). Submarine landslides are most of the times subcritical, which

*Corresponding author:
Jang-Jun Bahk
Department of Oceanography and Ocean Environmental Sciences, Chungnam National University, 99 Daehak-ro, Yuseong-gu, Daejeon 34134, Republic of Korea
Tel: +82-42-821-6433, Fax: +82-42-822-8173, E-mail: jjbahk@cnu.ac.kr

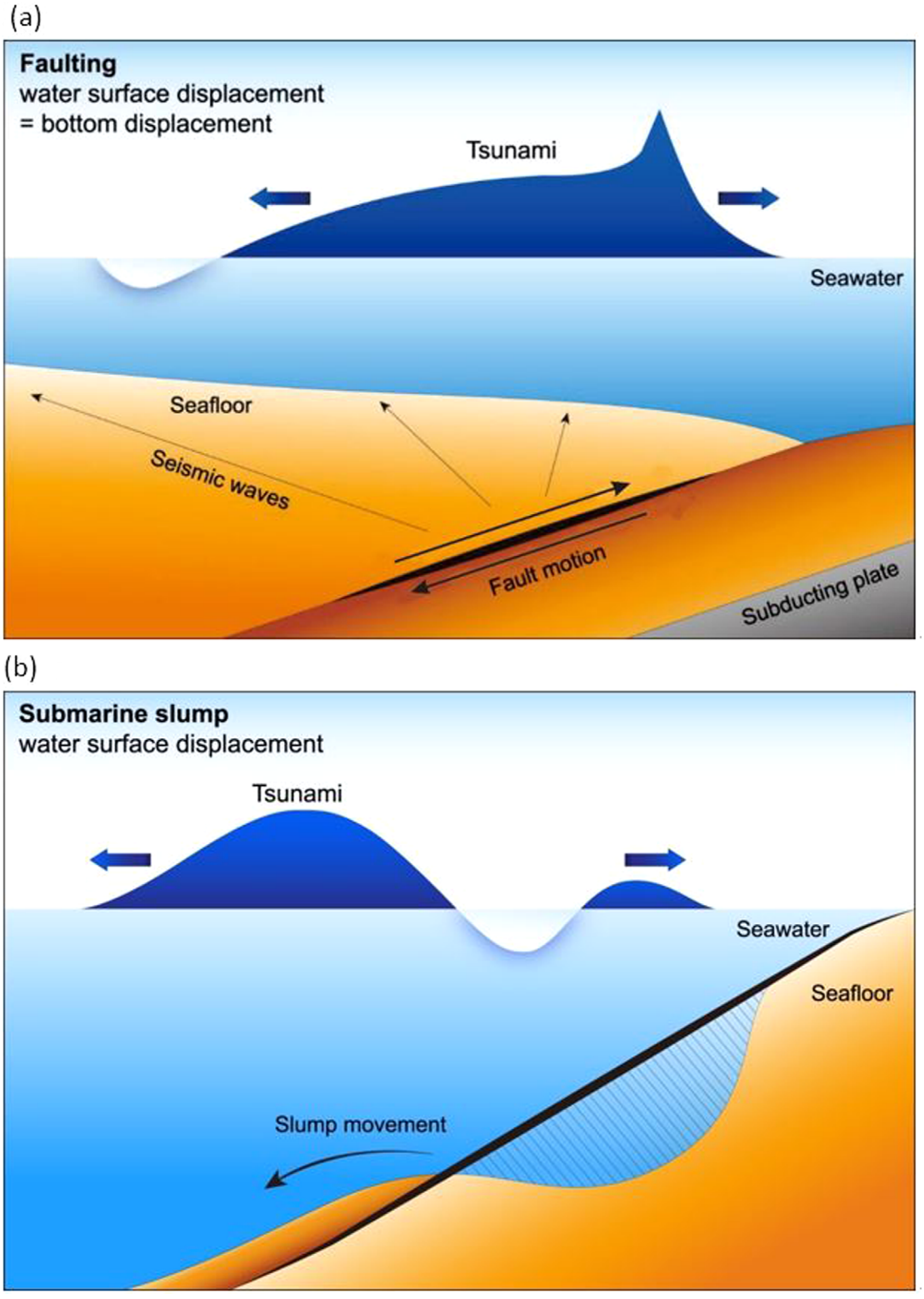

Fig. 1. Schematic diagram showing different tsunamis generation by earthquakes-faulting (a) and landslide (b). Modified from Satake and Tanioka (2003).

implies that the tsunami will run away from the wave-generating landslide (i.e., the tsunami travels faster than the landslide), limiting the build-up of the wave. However, for a landslide occurring in shallow water, effects of critical landslide motion (Froude number = 1) give large localized waves as illustrated by Ward (2001), resulting in more hazardous waves than if the

same landslide occurred in deep water. There is also a strong directivity along the landslide axis of motion (Fryer et al., 2004; Enet and Grilli, 2007; Waythomas et al., 2009) that often results in the focused local runup (e.g., Ruffman, 1997; Tappin et al., 2008), the magnitude of which is a function of tsunami source location, initial wave amplitude, and wavelength. The 1929 Grand Banks event (13 m) (Fine et al., 2005), the 1998 Papua New Guinea event (15 m) (Tappin et al., 2008) and the 1979 Nice event (3 m) (Assier-Rzadkieaicz et al., 2000) are just three examples of historical submarine landslide tsunamis that had large run-up heights locally. Earthquakes and tsunamis may also operate in combination to augment the damaging character of the resulting tsunamis. Hereof, it is to note that during the 2011 Tohoku earthquake and tsunami, the exceptionally high tsunami runups of up to 40 m recorded along the central Sanriku coast between 39.2°N and 40.2°N have been explained with an additional tsunami source, a submarine landslide located almost directly east of the central Sanriku coast (Tappin et al., 2014).

Tsunami risk assessment for the Korean coasts is based entirely on earthquake scenario simulations (Lim et al., 2008 and references therein), despite large submarine landslides are widely present on the western and southern slopes of the Ulleung Basin (Lee et al., 1999). As indicated above, tsunamis from submarine landslides have been largely ignored in the past, but estimates indicate that they could actually account for a significant portion of the tsunami record (Gusiakov, 2003; Tinti, 2003; Grilli et al., 2009; Harbitz et al., 2014). In Korea, many coastal communities, harbors and ports, as well as key industrial facilities are located along the eastern coast. Furthermore, 18 reactors at three nuclear power plants are now operating on the eastern coast, and several more plants are under construction (Choi et al., 2016). For nuclear applications, the annual design probability can be as low as 10^{-4} to 10^{-6} (Nicholson et al., 2013), corresponding to events with a mean return period in between 10 kyrs and 1 Myrs. Tsunami hazard assessment at those very low probabilities calls for inclusion of submarine landslides in the analysis (Geist and ten Brink, 2012), particularly when large slope failures, such as those along the Korean side of the East Sea, have been extensively mapped. The US Nuclear Regulatory Commission considers submarine landslides as the most likely source of tsunami in the US Eastern coast (Nicholson et al., 2013). Recurrence information for submarine landslides is however uncertain or altogether lacking in Korea, resulting in high uncertainty in the source term for probabilistic analysis, compared to earthquake recurrence. When data is not sufficiently available to establish a reliable distribution of submarine landslides, which is a major obstacle for a Probabilistic Tsunami Hazard Assessment (PTHA), a deterministic data-driven approach based on the worst-case credible scenario without the benefit from the underlying statistical distributions is the only feasible alternative (Harbitz et al., 2014).

The aims of this study are therefore to (1) highlight potential

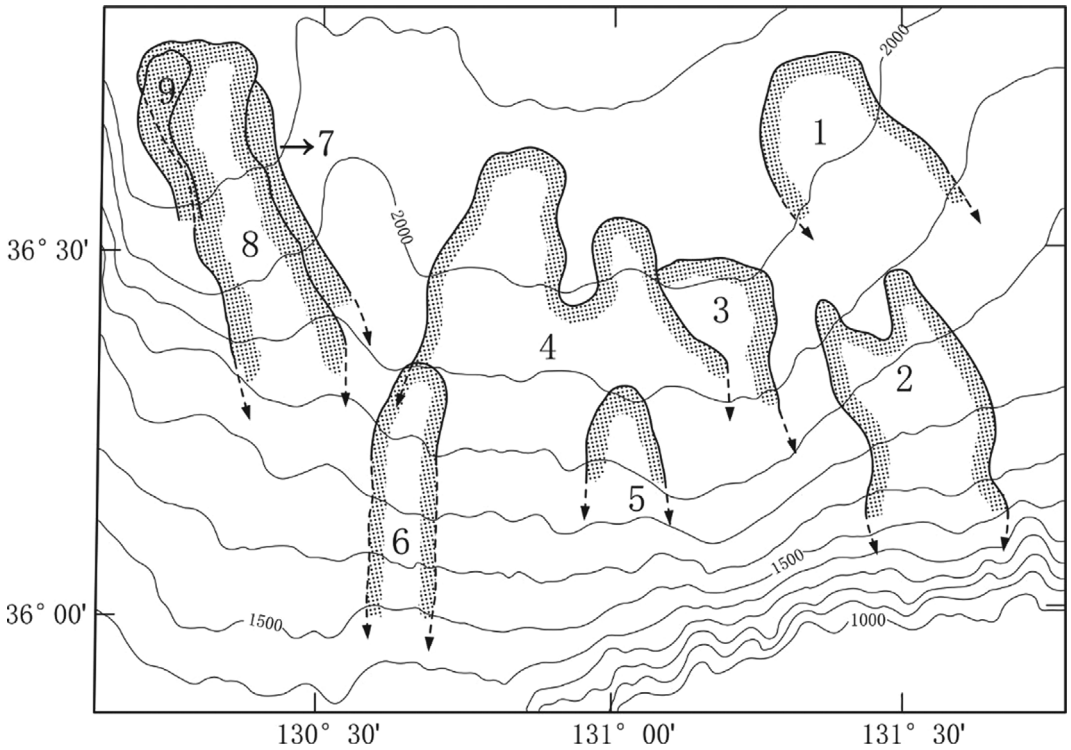

Fig. 2. Distribution of debris lobes in the southern Ulleung Basin based on mapping of high-resolution seismic profiles. Modified from Lee et al. (1999).

https://doi.org/10.1007/s12303-018-0044-x

tsunami hazard from submarine landslides on the Korean coast of the East Sea using scenario-based approaches and (2) assess the need for a Probabilistic Tsunami Hazard Assessment (PTHA) for the eastern coast of Korea focused on submarine landslides.

2. CHARACTERISTICS OF SUBMARINE LANDSLIDES IN THE ULLEUNG BASIN

Late Pleistocene slope failures on the western and southern continental slopes of the Ulleung Basin have disparate characteristics. Slope failures originating from the western margin have relatively small dimensions, while on the southern margin slope failures are at least one order of magnitude larger and may travel for several tens of kilometers along the slope and Ulleung Basin plain (Lee et al., 2014). The differences in failure volume are thought to result from variations in sediment supply, with the southern margin displaying much higher sedimentation rates, particularly during the glacial periods (Lee et al., 2014). Lee et al. (1999) identify at least 9 major Late Pleistocene debris flow events originating from slope failure of the southern margin with minimum volume estimates attaining up to 33.6 km^3 and minimum run-out distances of up to 127 km (Fig. 2). To provide a scale of these events, it is worth noting that the largest of these event covers an area of 1319 km^2, implying 1% of the territory of the Republic of Korea on-land.

Detailed side-scan sonar imaging and sediment coring of debris flow 8 (Fig. 2) have shown that these large debris flow lobes may actually result from multi-staged slope failure (Lee et al., 2013). Up to eight individual sedimentary bodies have been found to constitute debris flow 8 in the Ulleung Basin, suggesting that emplacement took place in a retrograding fashion in between 20.0 and 17.0 cal. ka B.P. Dating of turbidite successions during the last 30 kyrs in the Ulleung Basin shows that slope failure of multiple sizes were frequent during sea level lowstands while the frequency and relative volume of these slope failures significantly decreased during the Holocene (Lee et al., 2010).

3. METHODS

3.1. Input Bathymetric Information

The bathymetric information used for tsunami modeling and to support the interpretations is based mainly on a grid file in longitude latitude coordinates at 0.0009° resolution both for the X and Y directions (Fig. 3). The 0.0009° resolution approximately corresponds to 100 m resolution in the Y direction and about 80 m in the X direction at the 37° latitude. The bathymetric data were acquired by the Korea Hydrographic and Oceanographic Agency (KHOA) during the multibeam bathymetric survey of the East Sea from years 1996 to 1997 for the "Basic Maps of the Sea" of

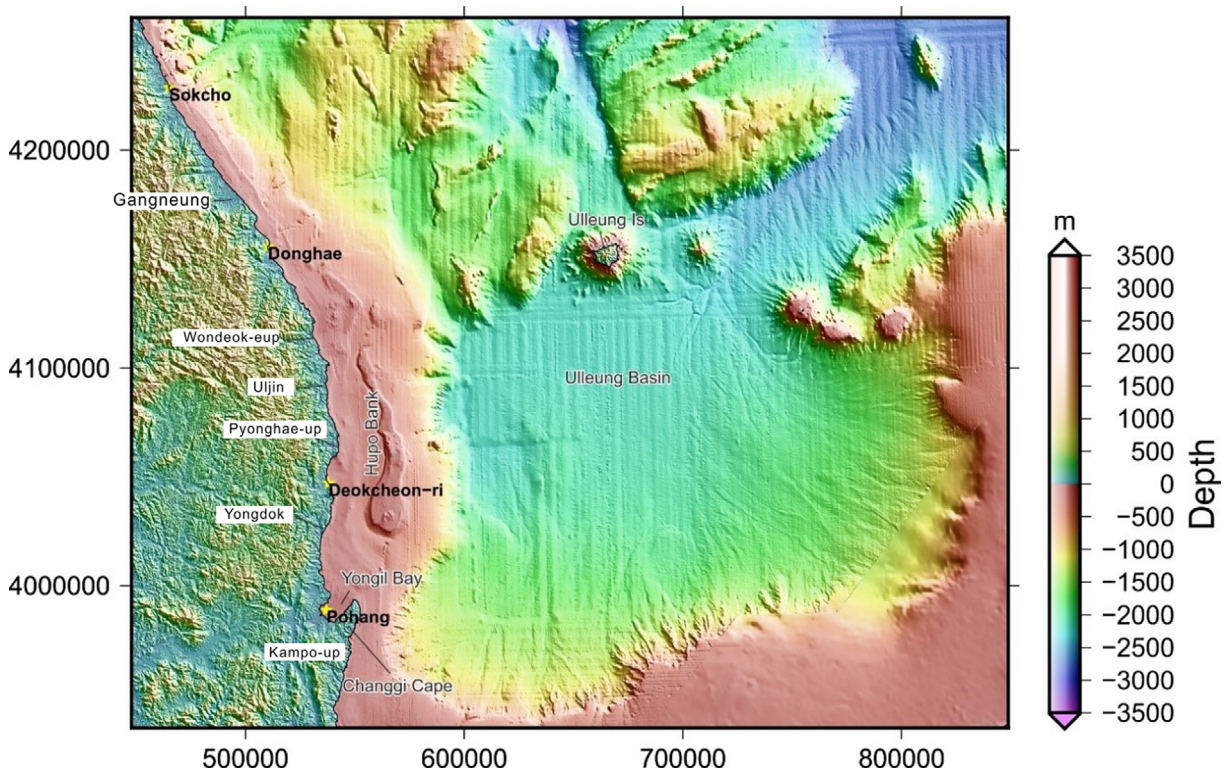

Fig. 3. Colored shaded relief image of the Ulleung Basin and adjacent Korean Peninsula. Elevation color scale is in meters. Stars show locations where numerical wave gauges have been placed to understand tsunami history. Locations referred to in the text are also shown.

Korea.

Missing elevation information in the multibeam bathymetric data set were filled with Shuttle Radar Topography Mission (SRTM) and ETOPO1 Digital Elevation Model (DEM) data. All data was converted to GMT (Wessel et al., 2013) 'netcdf' format sampled to the resolution of the multibeam data set, merged in one single grid file (Fig. 3) and converted to UTM coordinates (zone 52N) using MIRONE (Luis, 2007).

3.2. Tsunami Wave Model

The tsunami wave model chosen for this study is Geowave (e.g., Watts, 1998; Watts et al., 2003). Geowave simulates tsunami generation, propagation, and inundation using a fourth order fully nonlinear, fully dispersive Boussinesq wave model with multiple wave dissipation mechanisms, wave breaking, and dry land overflow (Wei et al., 1999; Chen et al., 2000; Kennedy et al., 2000). Geowave provides a programming architecture to generate multiple tsunami sources with TOPICS (Grilli and Watts, 1999, 2005; Grilli et al., 2002; Watts et al., 2005) and to insert those tsunami sources at the appropriate time into a simulation run in a modified version of FUNWAVE (Wei and Kirby, 1995; Chen et al., 2000).

This study employed the source code made available to registered users of Geowave that was compiled under a Linux environment using 'gfortran'. Simulation results were visualized using a series of C-shell scripts and the Generic Mapping Tools (Wessel et al., 2013). The only modifications made to the source code relate to the dimensions of the input grid (800 × 800 in the original code versus 4000 × 4000 in the code used for this exercise), the number of time steps (8001 in the original code versus 15000 in the code used for this exercise) and the sponge layer thickness at the edges of the simulation domain (10 in the original code versus 25 in the code used for this exercise). Sponge layers are used at oceanic domain boundaries to damp the energy of outgoing tsunami waves. Tide gage records have been computed at 4 stations along the Korean coast: from north to south these are Sokcho (11.8 meters water depth (mwd)), Donghae (0.8 mwd), Deokcheon-ri (1.5 mwd) and Pohang (15.8 mwd) for a simulation time of 65 minutes. (Stars in Fig. 3).

4. RESULTS

The work presented here concentrates on assessing tsunami hazard from submarine landslide sources in the western and southern shores of the Ulleung Basin based on three different scenarios (Table 1, Figs. 4, 5, and 6). Due to their proximity to the Korean coast, landslide tsunami sources originating in these areas are most likely to create damage to coastal settlements and infrastructures. These landslide tsunamis are likely to induce

Table 1. TOPICS input and output data

Landslide			Case 1	Case 2	Case 3
Landslide geometry	V	(km^3)	2.53	1.12	15.1
	x_o	(m E)	548508.9	586145.7	586525.9
	y_o	(m N)	4157191.6	4010600.9	3954703.3
	d	(m)	700	1290	934
	L	(km)	12.8	4	12.6
	l	(km)	7.6	3.5	14.4
	w	(m)	26	80	83
	φ	(°)	322.5	238.6	332
	θ	(°)	2	6	2.2
Landslide dynamics	a_i	(ms^{-2})	0.08	0.25	0.09
	v_t	(ms^{-1})	67.3	65.1	70.0
	t_c	(s)	794	256	751
	d_c	(km)	23.2	16.7	53
Initial tsunami	λ_c	(km)	78.6	28.8	71.9
	C_i	(m)	0.31	0.48	1.33
	T_i	(m)	−0.88	−1.07	−3.56

Notes: The longitude and latitude of the submarine landslide centroid (x_o, y_o) are the supposed center of mass; The centroid initial depth d (before the slide) corresponds to the depth of the scar center minus half of the maximum thickness w; The length L (Long axis) and width l (small axis) of the submarine landslide supposed-parallaloid; The mean azimuth (direction of landslide) φ defined counter-clockwise and the mean slope θ along slide.

TOPICS outputs are: the slide initial acceleration a_i, terminal velocity v_t and its characteristic duration tc (the wave period relative to the wave celerity at the centroid depth), the characteristic distance d_c and the characteristic initial tsunami wavelength λ_c. C_i and T_i represent the initial crest and trough amplitudes, respectively.

https://doi.org/10.1007/s12303-018-0044-x

higher runup than landslide tsunamis originated elsewhere in the basin, while timing for early warning will be the shortest. The simulations carried out in this study produce tsunami scenarios based on actual submarine landslides. These simulations attempt to present the significance of such events in determining hazard to coastal settlements and infrastructure and produce an overview of the consequences of landslide tsunamis for the Korean coast of the East Sea. The three case-scenarios are:

1. a Late Pleistocene submarine landslide north of the Hupo Bank on the continental slope west of the Ulleung Basin (Fig. 4).

2. a Late Pleistocene submarine landslide south of the Hupo Bank on the continental slope west of the Ulleung Basin (Fig. 5).

3. a Late Pleistocene submarine landslide on the continental slope south of the Ulleung Basin (corresponding to debris flow lobe 8 of Lee et al., 1999; Fig. 6).

Each scenario considered individually, represents a worst-case submarine landslide scenario, as the slope failure is assumed to be triggered as a single stage slide (see Table 1 for geometric and geographic characteristics of the submarine landslides that made the different scenarios). Nevertheless, the third scenario is considered the basin worst case scenario, as the landslide has a series of characteristics that could result in relatively high tsunami waves arriving at the Korean shore in a relatively short time. Amongst those characteristics, the landslide is one order of magnitude larger than the two former, it occurs in relatively shallow waters (see Table 1) and, quite importantly, it is the landslide closest to the Korean Peninsula among those led to the debris lobes of the 10–100 km^3 magnitude range in the southern Ulleung Basin (Fig. 2), providing the shortest time for early warning with little damping of tsunami wave amplitude.

The slide approximation used in Geowave is probably correct for the initial stages of slope failure, which have most influence in tsunami generation (Watts et al., 2005; Harbitz et al., 2006; Enet and Grilli, 2007; Løvholt et al., 2015). However, the initial slides most likely disintegrated to form a debris flow as observed in many instances in the Ulleung Basin (e.g., Lee et al., 1999, 2013).

Geometric landslide parameters derived from bathymetric cross-sections of each landslide (Figs. 4, 5, and 6) and initial tsunami wave properties for each scenario are given in Table 1. The tsunami simulations carried out for this exercise were performed with the Present-day sea level as free surface elevation datum. Nevertheless, at the time of occurrence of the various simulated submarine landslides, the sea level could differ from the Present one. Therefore, the simulations highlight the consequences should one of these failures occur at Present and not what actually happened at the timing of occurrence of these slope failures. On top of that, the tidal stage during a tsunami cannot be predicted

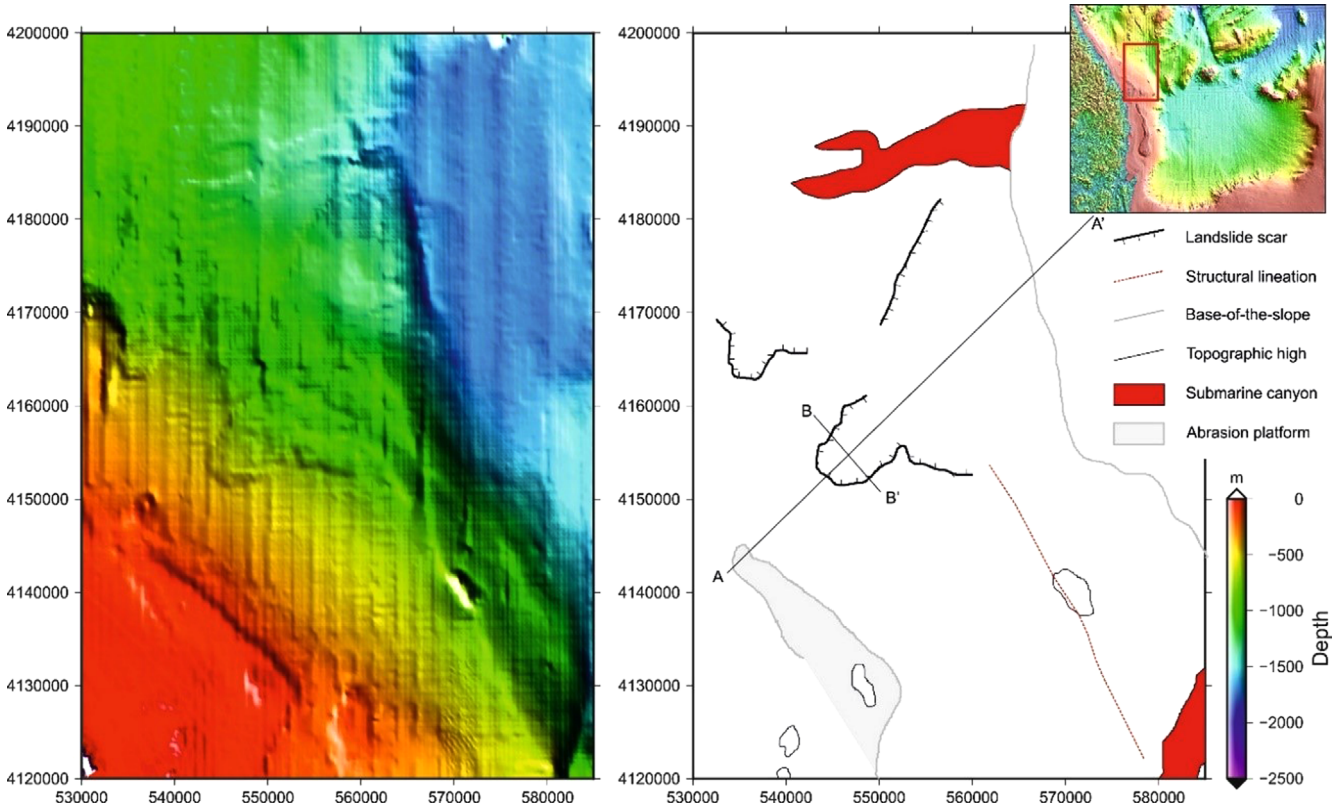

Fig. 4. Colored shaded relief image and geomorphological interpretation portraying Case 1 submarine slope failure. Bathymetric cross-sections for estimation of geometric landslide dimensional parameters in Table 1 are located.

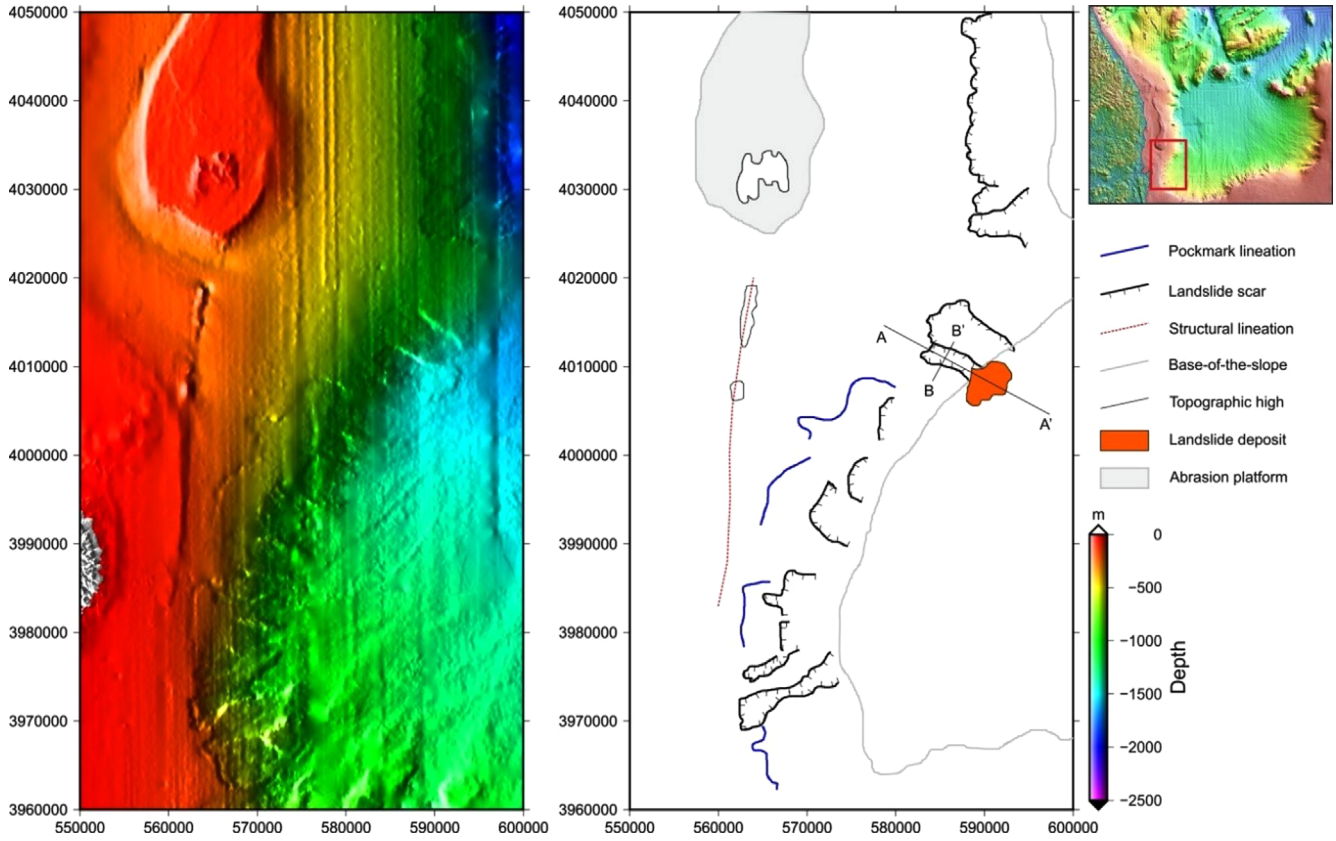

Fig. 5. Colored shaded relief image and geomorphological interpretation portraying Case 2 submarine slope failure. Bathymetric cross-sections for estimation of geometric landslide dimensional parameters in Table 1 are located.

and is, therefore, a source of uncertainty (Mofjeld et al., 2007).

4.1. Case 1: Submarine Landslide North of the Hupo Bank

The first tsunami scenario is the result of a slope failure on the continental slope west of the Ulleung Basin immediately north of the Hupo Bank. This landslide is similar in characteristics to the one identified by Cukur et al. (2016) with higher resolution bathymetric data and complete set of geophysical information. The slope failure occurs in water depths of 400 to 900 meters below sea level (mbsl) and results in an arcuate shaped embayment on the slope that is 7.6 km wide and 12.8 km long (Fig. 4). The landslide scar is relatively constant in height (~26 m) and the failure plane is parallel to the slope, which indicates that the failure most likely initiated as a slide (Fig. 4). The failure occurred on a very gentle slope of only 2° and no deposits can be observed on the bathymetric data associated to the landslide scar. This indicates that the initial slide likely disintegrated to form a debris flow that travelled all the way to the Ulleung Basin. The submarine landslide characteristics, modeled by Geowave indicate an initial acceleration (a_i) of 0.08 ms^{-2}, a terminal velocity (v_t) of 67.3 ms^{-1}, a characteristic time (t_c) of 794 s and a characteristic distance (d_c) of 23.2 km.

The terminal velocity of the landslide v_t is the maximum velocity that a submarine landslide can attain due to the drag force exerted by water, with thicker slides attaining a higher speed (Enet and Grilli, 2007; Xiao et al., 2015). Based on the equations of motion given by Watts (1998) and Watts et al. (2000) we estimate that the terminal velocity (v_t) of the center of the slide was reached at the base of the slope at ~1700 mbsl. The phase speed of a tsunami (or its celerity) in water H = 1700 m deep, is $\sqrt{dg}$ = 130 m/s. The higher tsunami velocity compared to the landslide means that, the landslide was not 'in phase' with the tsunami it was generating, and therefore it was not efficient in building a large size tsunami (Tinti and Bortolucci, 2000; Fryer et al., 2004).

The characteristic time t_c designates the moment after failure when the wave build-up is finished and transformation of potential energy into kinetic energy takes place (Brune et al., 2010). It is defined as $t_c = v_t / a_i$. The characteristic time of motion t_c plays a special role as it designates the moment, when the initial tsunami shape is introduced as starting condition to the tsunami propagation model. The characteristic distance d_c roughly

https://doi.org/10.1007/s12303-018-0044-x

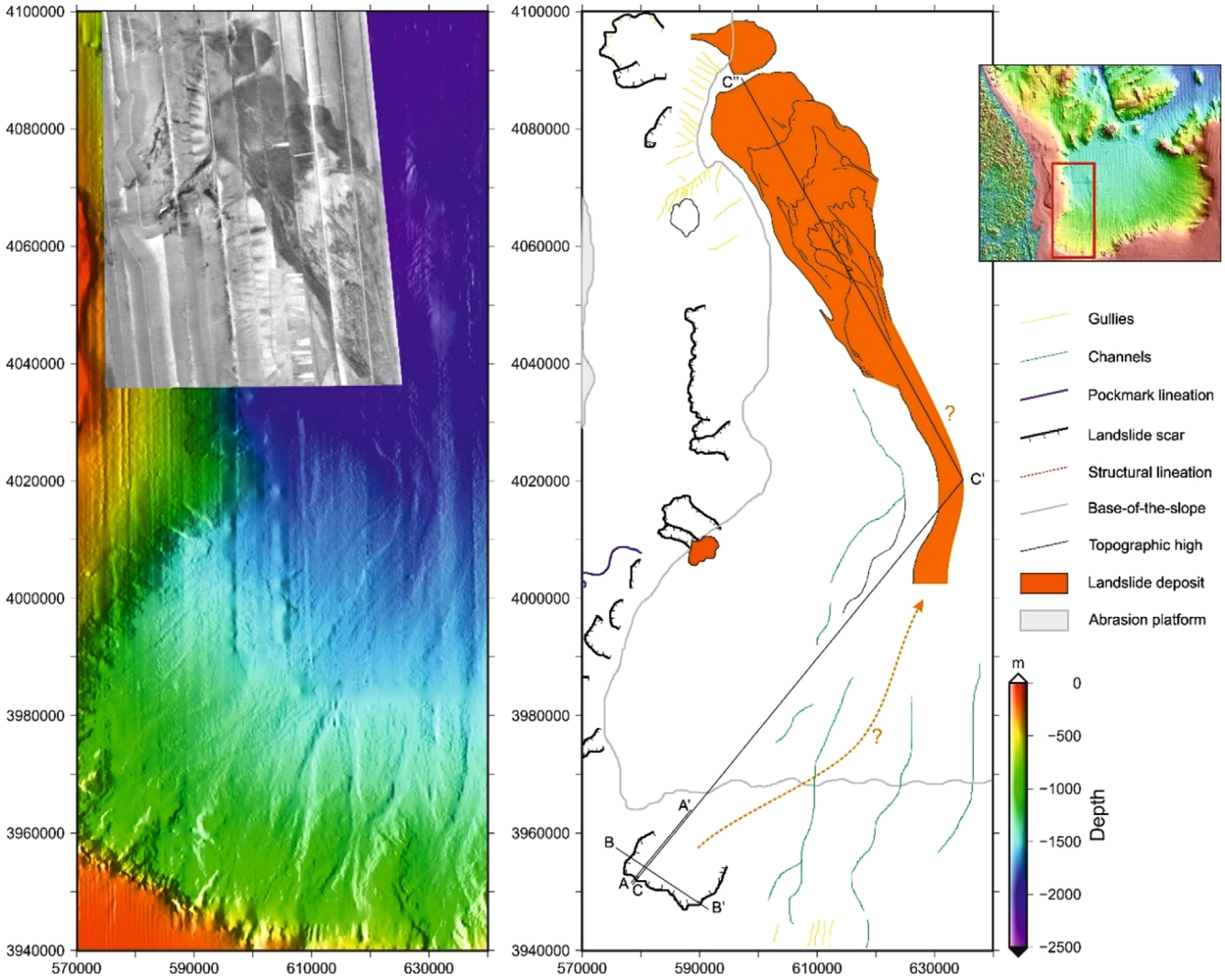

Fig. 6. Colored shaded relief image with geo-referenced MR1 side-scan sonar mosaic (from Lee et al., 2013) and geomorphological interpretation portraying Case 3 paleo-submarine slope failure. Bathymetric cross-sections for estimation of geometric landslide dimensional parameters in Table 1 are located.

approximates the landslide runout distance, although part of the slide mass can travel farther as a turbidity current.

The output of the simulation of this landslide-generated tsunami north of the Hupo Bank allows to measure free water surface changes at any point along time (Fig. 7). The height wave plots show that the landslide produces a dipole wave with a trough (blue for elevations lower than –0.1 m in Fig. 7) located over the sediment failure area in the upper slope and an adjacent high (red for elevations higher than 0.1 m in Fig. 7) to the northeast. Water elevations in between –0.1 and 0.1 m are shown in white to highlight the highest amplitudes, but the shading in the images shows actual tsunami activity within this elevation interval. This initial wave radially spreads and progressively deforms, acquiring a more circular shape. The Ursell number ($Ur = C_i\lambda^2/d^3$), where C_i is the maximum wave amplitude and λ is the characteristic wavelength (Murty, 1977), allows to assess the relative importance of nonlinear and dispersive effects during water wave propagation. For typical amplitudes and wavelength of the tsunami as well as water depths in that area of the basin, it can be seen that dispersion played a role in tsunami propagation.

To the southwest the tsunami wave train advances toward the Korean Peninsula at a significantly slower speed, greater amplitude and smaller wavelength than the outgoing wave, directed toward the center of the basin (Fig. 7). Such outgoing wave impacts the Ulleung Island ~20 minutes after landslide initiation (Fig. 7). The slower back-going tsunami reaches the Korean Peninsula ~30 minutes after onset of the landslide, first reporting a negative amplitude as shown by the Donghae and, 5 minutes later, by the Sokcho synthetic wave gage (Fig. 8). At these two locations the first wave was the highest and arrived with relatively small

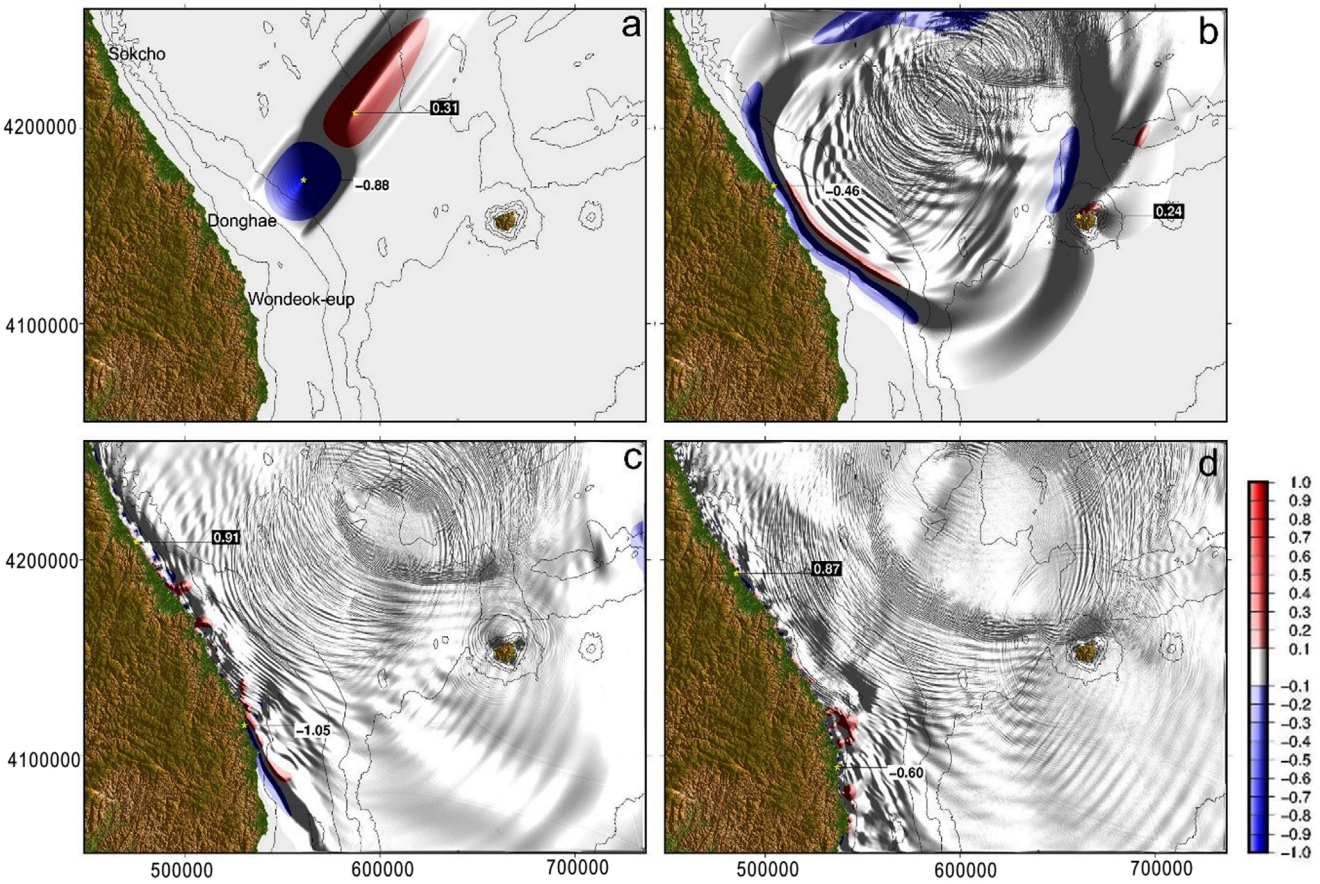

Fig. 7. (a) Colored shaded relief image of initial surface elevation generated by TOPICS for the submarine landslide in Case 1. Free surface elevation at 25 min (b), 37 min (c) and 49 min (d) after onset of submarine slope failure. Tsunami color scale is in meters. Background black lines show bathymetric contours (with the 100, 500, 1000 and 2000 m iso-contours).

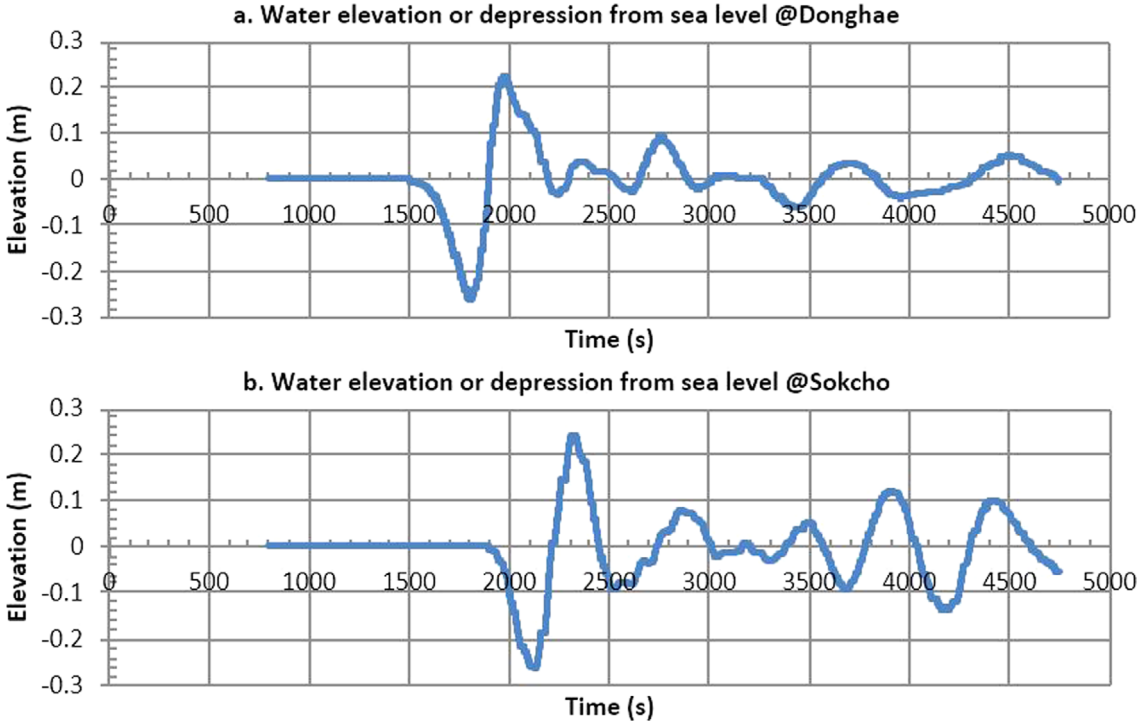

Fig. 8. Time series of tsunami elevation at the Donghae (a) and Sokcho (b) numerical wave gauges set in 0.8 and 11.8 meters water depth respectively. See Figure 3 for location of numerical wave gauges.

https://doi.org/10.1007/s12303-018-0044-x

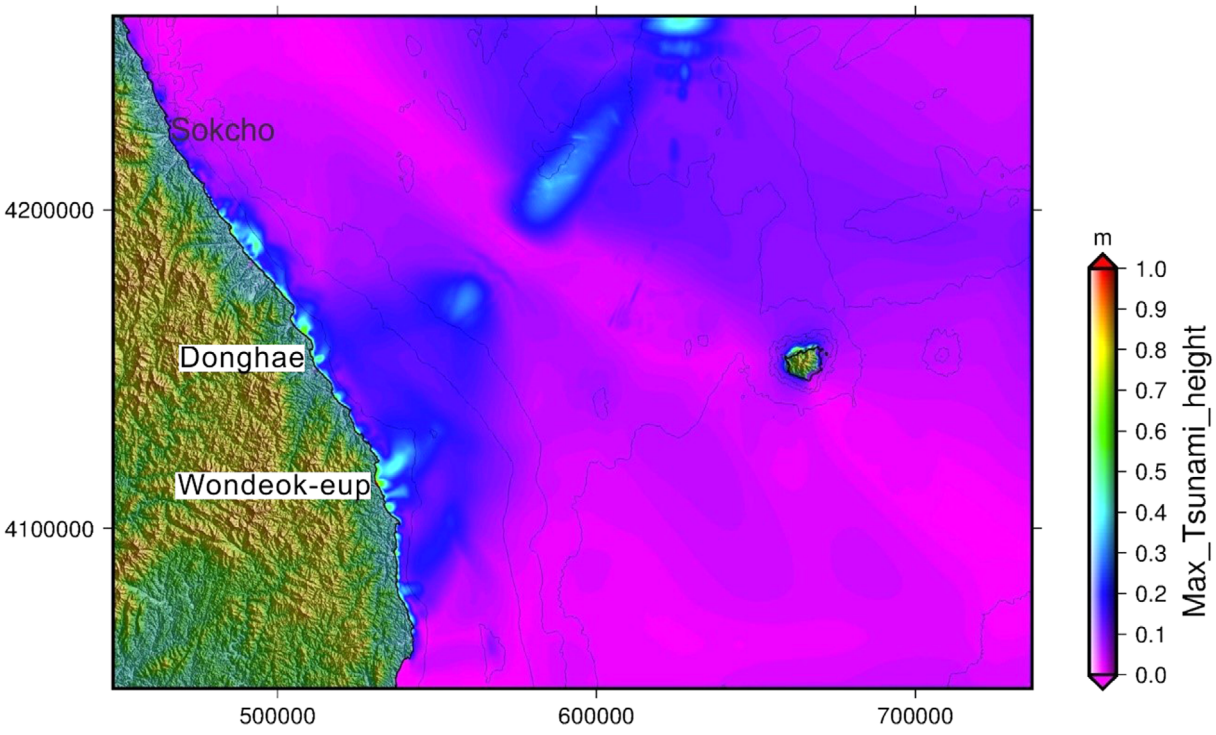

Fig. 9. Color image of maximum elevation in meters above sea level at any time during the numerical simulation for the underwater landslide in Case 1. North is oriented up. Simulated on a 80 m grid. Tsunami color scale is in meters. Background black lines show bathymetric contours (with the 100, 500, 1000 and 2000 m iso-contours).

amplitudes of 20–25 cm. The tidal gage plots show that subsequent waves arrived periodically at 5–8 minutes intervals with slightly lower amplitude (Fig. 8). The maximum elevations plot (Fig. 9) shows the maximum free surface elevation reached at each cell during the entire simulation. Most values range from 0 to 0.4 m, with a mean elevation of 0.2 m. Wave elevation peaks close to 2 m are observed near the coastline, particularly for the stretch of coastline 20 km south of Uljin to 20 km north of Gangneung. The maximum elevation reached by the first tsunami wave arrival is found ~5 km north of Donghae, where records indicate a 1.6 m wave. However the highest free surface elevation is reached near Wondeok-eup, Samcheok-si, Gangwon-do near the border with the Gyeongsangbuk-do region with 1.9 m (Fig. 9). In this case the wave does not result from the direct tsunami arrival, but from subsequent tsunami reflections, refractions and diffractions.

This work does not provide a detailed analysis of the runup and inundation effects of the tsunami waves on shore, but based on the average 0.2 m wave height over the shelf, a generalized tsunami runup of up to 2.5 m can be expected for beach profiles with a gentle slope of 1° (Synolakis, 1987), which reduces to 1.6 m for a beach with a slope profile of 3°.

In the central stretch of coastline in between Uljin and Donghae, it takes about 25 minutes for the tsunami waves to reach the coastline. In about 1 hour the tsunami has reached most of South Korea's shore of the East Sea. With regard to the timing of arrival of the highest tsunami wave, Figure 10 shows that, in the same central stretch of coastline in between Uljin and Donghae, the highest tsunami waves arrived with the first tsunami arrival, ~25 minutes after tsunami initiation. However, the time of highest tsunami arrival for locations along the coastline to the south and north of the first impact zone is significantly larger than the initial tsunami arrival time (Fig. 10). This indicates that reflected and refracted tsunami waves arrived in these areas of the coast with higher amplitude than the first tsunami arrival.

4.2. Case 2: Submarine Landslide South of the Hupo Bank

This tsunami scenario results again from a slope failure on the continental slope west of the Ulleung Basin, but in this case to the south of the Hupo Bank, where the continental slope defines a reentrant characterized by multiple slope failures (Fig. 5). A distinctive feature of landslides in this reentrant to the south of the Hupo Bank is an arcuate depression near the shelf edge. The origin of this feature is not clear with bathymetric data alone, but could be linked to fluid expulsion to the seafloor. A potential cause-effect relationship may exist between the fluid expulsion and the landslides, suggesting that new submarine landslides

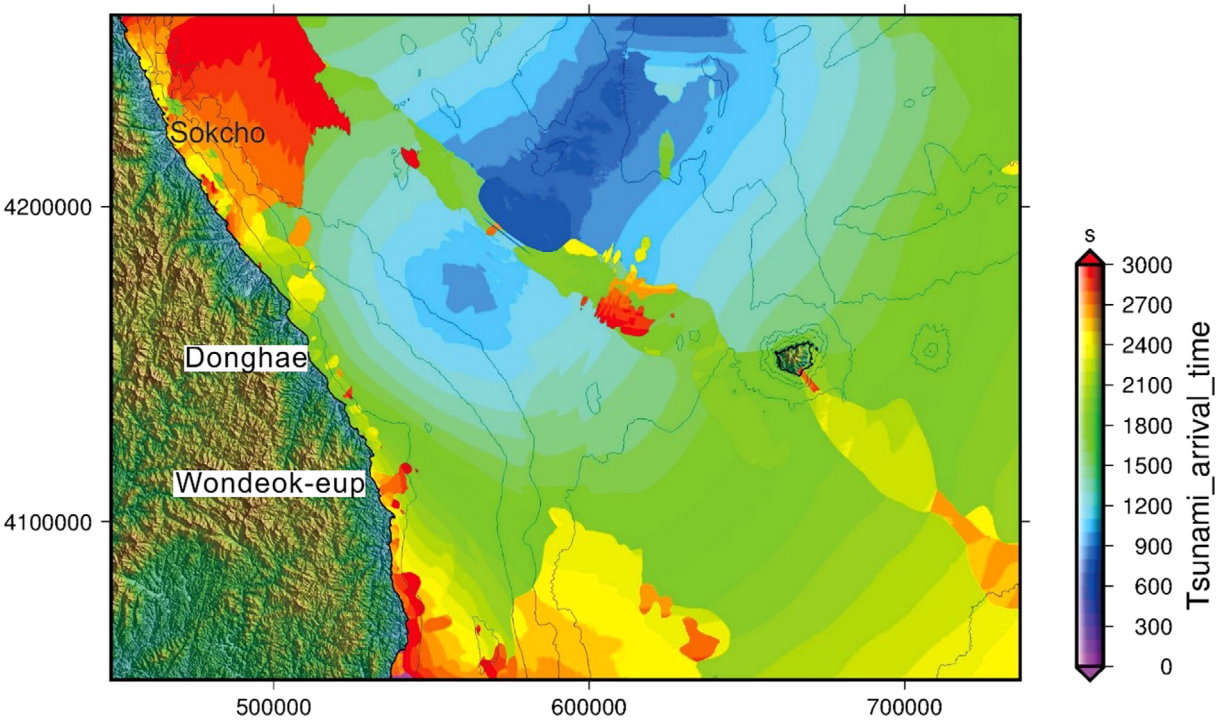

Fig. 10. Color image showing timing of arrival in seconds of maximum tsunami wave amplitude for the underwater landslide in Case 1. North is oriented up. Simulated on a 80 m grid. Tsunami color scale is in meters. Background black lines show bathymetric contours (with the 100, 500, 1000 and 2000 m iso-contours).

could be expected in the area in the future (Fig. 5). The slope failure of this case occurred immediately north of this reentrant in water depths between 1000 to 1600 mbsl and resulted in a horseshoe scarp on the slope that is 3.5 km wide and 4 km long (Fig. 5), i.e., a significantly smaller landslide in deeper water depths. The landslide scar affects however a significantly larger package of sediments involving a total thickness of ~80 m. The failure plane seems also parallel to the slope indicating an initial failure style as a slide (Fig. 5). The slope occurred on a comparatively steeper slope averaging 6° and a body of sediment seems visible on the bathymetric data at the foot of the landslide scar, indicating that the initial slide again disintegrated to form a debris flow that came to rest at the foot of the scar (Fig. 5).

The submarine landslide characteristics modeled by Geowave indicate an initial acceleration (a_i) of 0.25 ms^{-2}, which is in agreement with the steeper slopes along that failure, a terminal velocity (v_t) of 65.1 ms^{-1}, a comparatively shorter characteristic time (t_c) and characteristic distance (d_c) of 256 s and 16.7 km respectively. The phase speed of the tsunami in water H = 1500 m deep, is $\sqrt{dg}$ = 121 ms^{-1}, which given the landslide terminal velocity implies a Froude number of 0.54 and a relatively low tsunami generating efficiency, which is typical for deep-water submarine landslides (Fine et al., 2003; de Blasio, 2011).

The output of the simulation for this landslide-generated tsunami is shown in Figure 11. The height wave plots show the characteristic initial dipole of landslide generated tsunamis with a wave trough at the location of the landslide scar on the slope and an adjacent high at the location where the landslide deposited the sediment involved in the slope failure (Fig. 11) to the northeast. The trough initially produced by the landslide is just 1.07 m deep, while the adjacent high is 45 cm in elevation. The tsunami's characteristic initial wavelength is 29 km. Both trough and high are initially elongated in the WNW-ESE direction and this initial wave radially spreads and progressively deforms, acquiring a more circular shape. The Ursell number for typical amplitudes (0.1–0.3 m) and wavelengths (10–25 km) of this tsunami in water depths exceeding 500 m is found to be small (< 1). This means that frequency dispersion effect dominates over nonlinear effect (or amplitude dispersion effect) at the source although, as the tsunami approaches the shore, the nonlinear effect must become increasingly important due to shoaling.

Due to the bathymetric configuration, the tsunami wave train advances over the shelf toward the Korean Peninsula at a significantly slower speed, greater amplitude and smaller wavelength than the outgoing wave, directed to the ESE (Fig. 11). The back-going tsunami reaches the Korean Peninsula near the Changgi Cape just ~15 minutes after onset of the landslide. The synthetic wave gages located in Deokcheon-ri and Pohang in 1.5 and 15.8 mwd (see Fig. 3 for location) both report initial negative amplitude 26 minutes in Deokcheon-ri and 33 minutes in Pohang after

https://doi.org/10.1007/s12303-018-0044-x

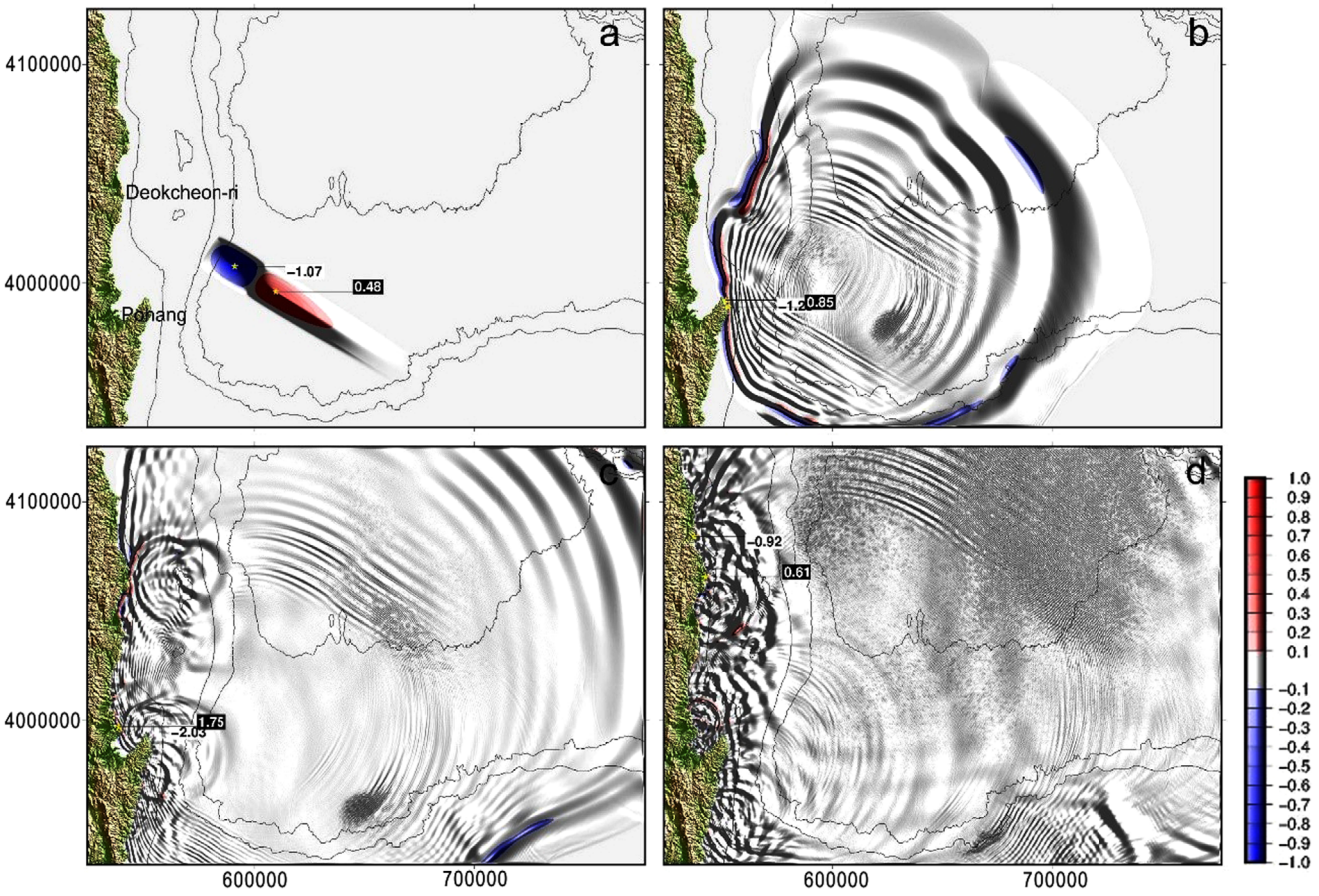

Fig. 11. (a) Colored shaded relief image of initial surface elevation generated by TOPICS for the submarine landslide in Case 2. Free surface elevation at 18 min (b), 31 min (c) and 45 min (d) after onset of submarine slope failure. Tsunami color scale is in meters. Background black lines show bathymetric contours (with the 100, 500, 1000 and 2000 m iso-contours).

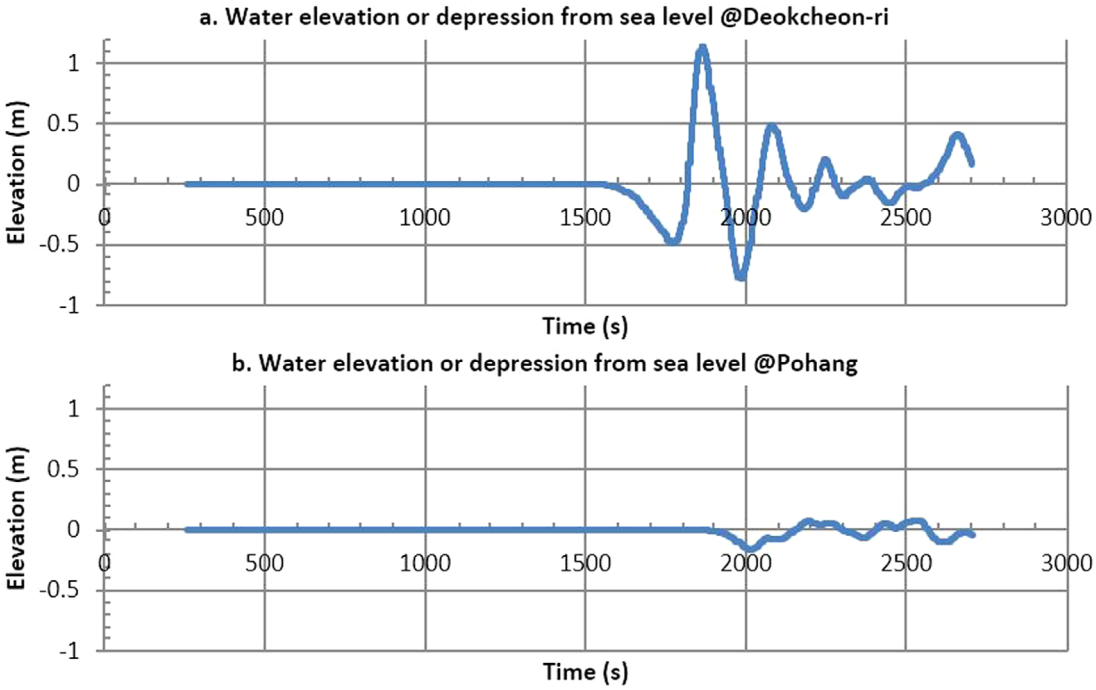

Fig. 12. Time series of tsunami elevation at the Deokcheon-ri (a) and Pohang (b) numerical wave gauges set in 1.5 and 15.8 meters water depth respectively. See Figure 3 for location of numerical wave gauges.

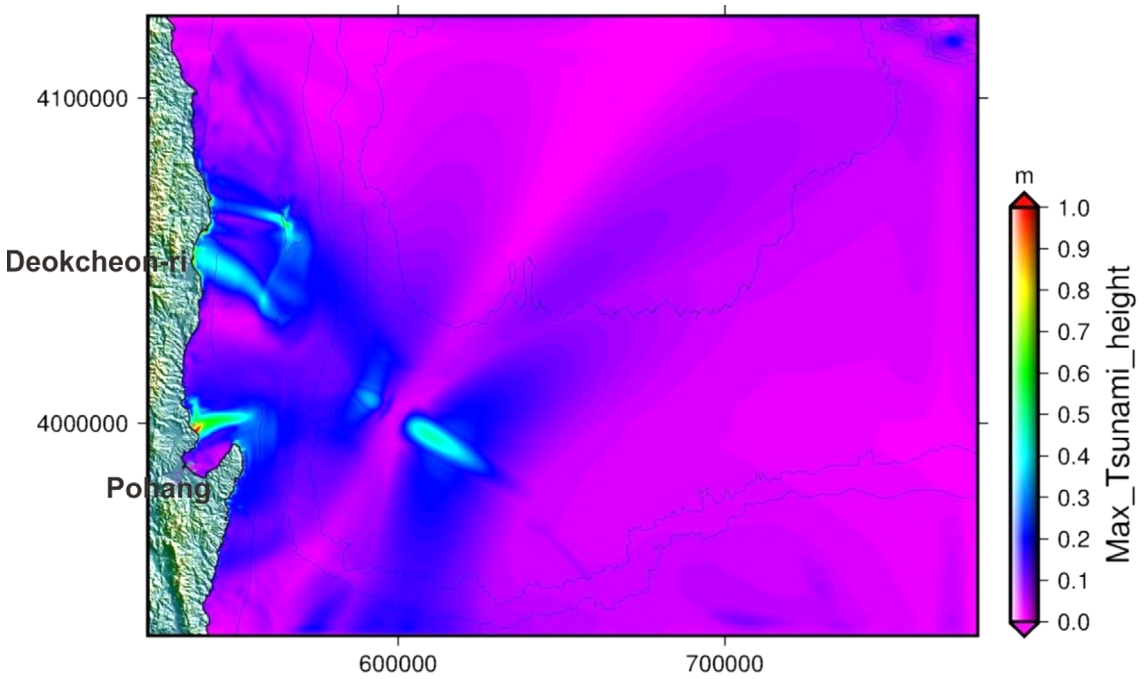

Fig. 13. Color image of maximum elevation in meters above sea level at any time during the numerical simulation for the underwater landslide in Case 2. North is oriented up. Simulated on a 80 m grid. Tsunami color scale is in meters. Background black lines show bathymetric contours (with the 100, 500, 1000 and 2000 m iso-contours).

onset of the landslide (Fig. 12). At Deokcheon-ri the first arrival wave was the highest and arrived with an amplitude of 1.1 m. The tidal gage plots show that subsequent waves arrived periodically at 3 minutes intervals with a wave amplitude of ~0.5 m (Fig. 12). However, at Pohang the wave amplitude was rather insignificant as the Yongil Bay was largely sheltered from the tsunami by the Changgi Cape (Fig. 12).

The maximum elevations plot for this tsunami (Fig. 13) shows most values not higher than 0.4 m. However, near the coastline, elevations often exceed 1 m and may reach up to 3.5 m. Here the bathymetric lows along the Hupo Bank have a significant effect in concentrating the tsunami energy at certain locations along the coastline, particularly in between Yongdok and Pyonghae. In a similar way diffraction of tsunami energy at the Changgi Cape concentrated the highest tsunami energy on the opposite side of the Yongil Bay (Fig. 13).

Estimating the runup using the empirical formulation of Synolakis (1987) does not seem to provide additional insight into the effects of the tsunami and the expected runups are well below the maximum wave amplitudes recorded by Geowave near the coastline. Similarly to the previous case, using an average 0.2 m wave height over the shelf a generalized tsunami runup of up to 2.5 m can be expected for beach profiles with a gentle slope of 1°, which reduces to 1.6 m for a beach with a slope profile of 3°.

The tsunami arrival (Fig. 14) was significantly faster (15 minutes) compared to the first landslide tsunami, north of the Hupo Bank (25 minutes). This shorter arrival time is largely due to the narrower shelf in this area of the East Sea (Fig. 3). The arrival time is particularly short on the east side of the Changgi Cape. However, in between Ulsan and Donghae the first tsunami arrival most often took in between 25 to 35 minutes. With regard to the timing of arrival of the highest tsunami wave, Figure 14 shows that in the eastern side of the Changgi Cape these maximum waves coincided with the first tsunami arrival, ~15 minutes after tsunami initiation. However, the arrival of the highest tsunami wave for some locations along the coastline to the south and north of the first impact zone and within the Yongil bay is significantly delayed with respect to the initial tsunami arrival time (Fig. 14). This indicates again that reflected and refracted tsunami waves arrived at the coast with higher amplitude than the first tsunami arrival.

4.3. Case 3: Worst Case Scenario. A Landslide in the Southern Margin of the Ulleung Basin

This last tsunami simulation presents a worst case scenario amongst all landslides in the basin and is based on results from Lee et al. (1999). These results show the presence of large Mass Transport Deposits (MTDs) on the floor of the Ulleung Basin that originated from the southern slope of the basin (Fig. 2). Later investigations by Lee et al. (2013, 2014) have however pointed

https://doi.org/10.1007/s12303-018-0044-x

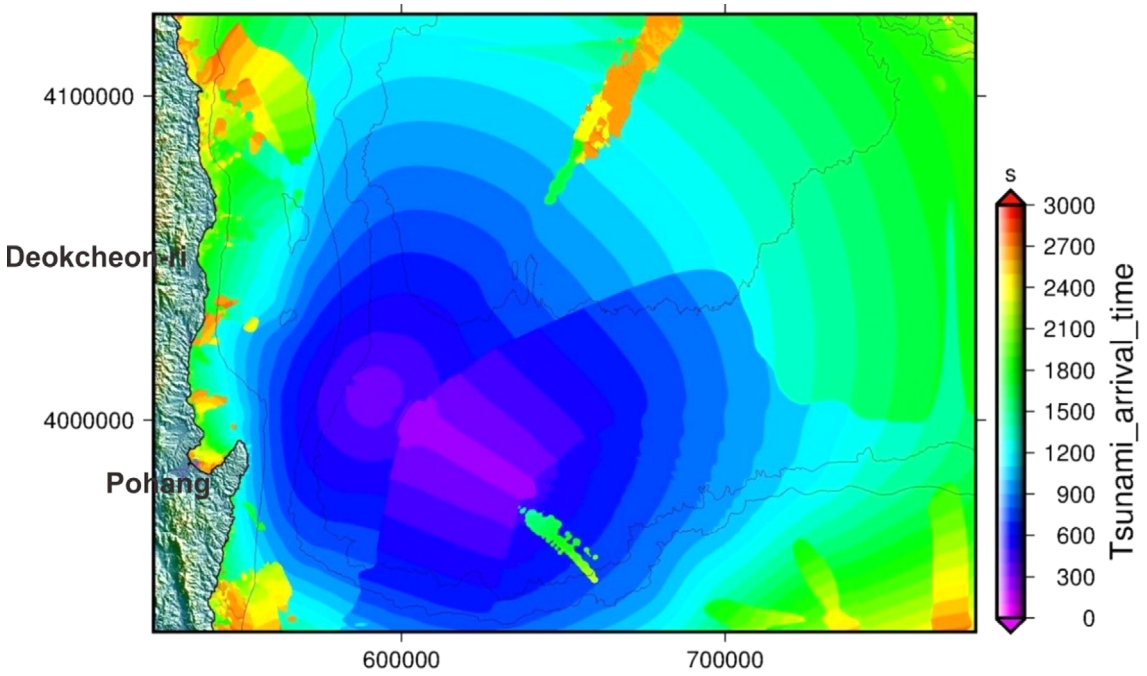

Fig. 14. Color image showing timing of arrival in seconds of maximum tsunami wave amplitude for the underwater landslide in Case 2. North is oriented up. Simulated on a 80 m grid. Tsunami color scale is in meters. Background black lines show bathymetric contours (with the 100, 500, 1000 and 2000 m iso-contours).

out that the MTD identified as Lobe 8 in Lee et al. (1999) could actually result from failure in various stages between 20 and 17 kyrs BP. The deposition of the various lobes in multiple stages has obvious implications for the size of the subsequent tsunami wave. Nevertheless, we choose here to model this scenario as the result of one single event to highlight the consequences of an extreme event. The occurrence of slope failures from the southern slope in multiple stages has been proven for lobe 8 of Lee et al. (1999), but nothing is known on the multi-staged nature of lobes 1 to 7 (Lee et al., 1999), which might have even larger volumes than lobe 8 (Fig. 2).

Figure 6 presents the HAWAII MR1 (the name stands for HIG Acoustic Wide-angle Imaging Instrument, Model Revision 1) side-scan sonar mosaic of Lee et al. (2013) geographically registered onto the bathymetric information. Upslope from the debris flow body (highlighted in orange in the interpretation of Fig. 6) a series of lineations on the bathymetric data seem to trace the debris flow to a series of not well-defined scarps near the shelf edge of the southern Ulleung Basin continental slope (Fig. 6). We hypothesize that this area is the source of the MTD and therefore simulate the tsunami as originating from it. To this purpose we have taken into account the sediment volume involved in the MTD (15.1 km^3 according to Lee et al. (1999)) and have used such volume for simulation of the slide.

The simulated slope failure occurs in water depths between 300 to 1000 mbsl, it is 14.4 km wide and 12.6 km long (Fig. 6) and involves a sediment thickness of ~83 m, i.e., a landslide one order of magnitude larger than the previous ones. Notice that landslides of such size are not infrequent in the marine environment (e.g., see catalogues in ten Brink et al., 2006; Chaytor et al., 2009; Urgeles and Camerlenghi, 2013) and may attain volumes up to several thousands of km^3 (e.g., the Storegga slide (Solheim et al., 2005), which tsunami deposits have been identified all over northern Europe (Bondevik et al., 2005)). The slope at the source area of the landslide is 2.2° on average.

At the initial position of the center of mass of the landside (water depth H = 930 m), the tsunami phase speed is $\sqrt{dg} = 95$ ms^{-1}, which implies a Froude number of 0.74 (Fine et al., 2003; de Blasio, 2011). This Froude number is slightly closer to the resonance value of 1 implying that the landslide was also a bit more efficient in building a tsunami wave compared to the previous cases.

The tsunami simulation for this Late Pleistocene landslide shows a much larger dipole than for the previous ones (Fig. 15). The wave trough centered on the landslide scar area is 3.5 m deep while the adjacent high is 1.3 m, which makes an initial tsunami amplitude 3 times larger than that of previous scenarios. Both trough and high are oriented NE-SW in the initial direction of landslide motion. The tsunami has a characteristic initial wavelength of 70 km. Both trough and high are initially elongated in the WNW-ESE direction. This initial wave radially spreads and progressively deforms, acquiring a more circular

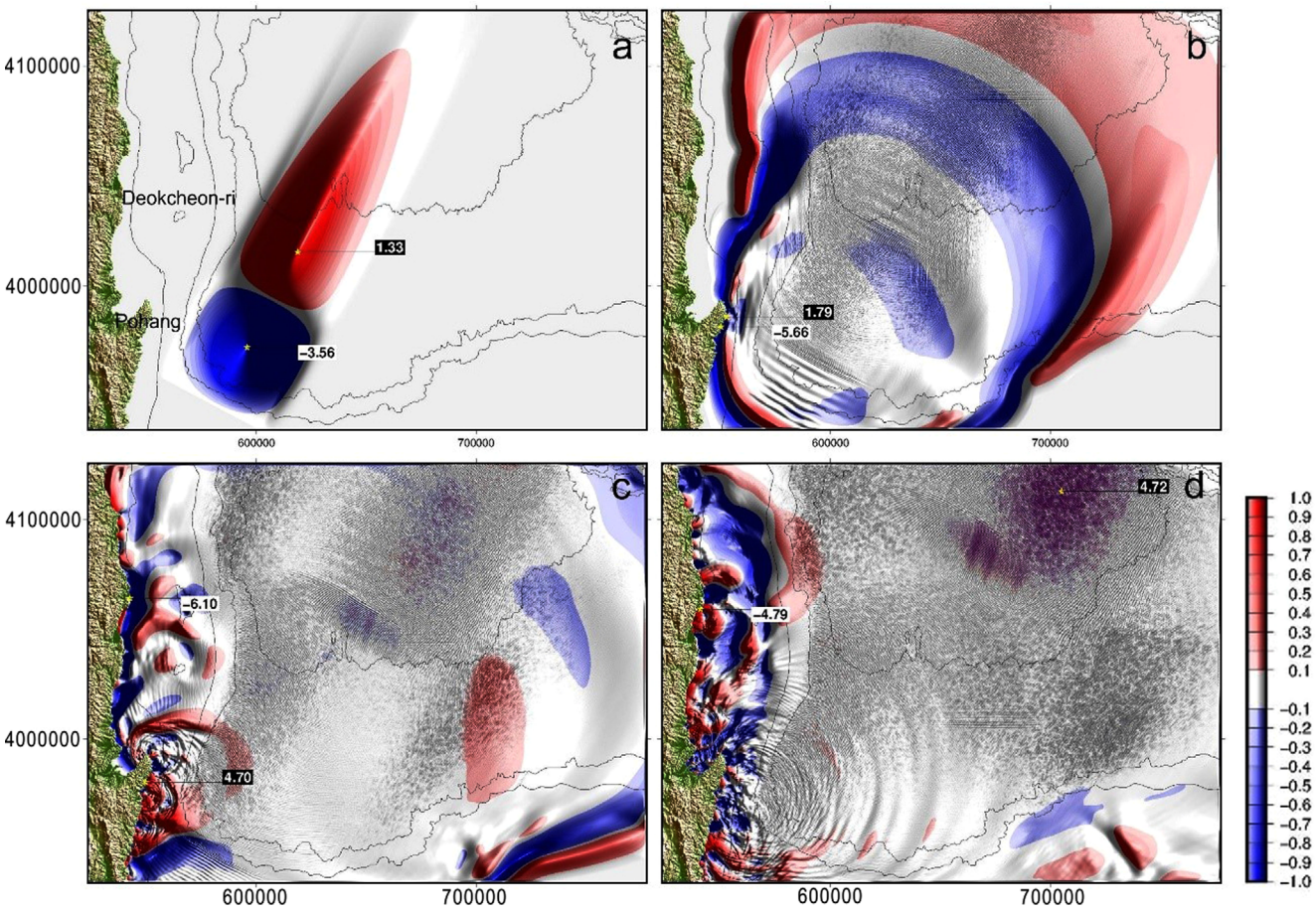

Fig. 15. (a) Colored shaded relief image of initial surface elevation generated by TOPICS for the submarine landslide in Case 3. Free surface elevation at 26 min (b), 40 min (c), and 53 min (d) after onset of submarine slope failure. Tsunami color scale is in meters. Background black lines show bathymetric contours (with the 100, 500, 1000 and 2000 m iso-contours).

shape. Large tsunami amplitudes and wavelengths imply that large Ursell numbers are obtained throughout the basin and therefore the nonlinear effect (or amplitude dispersion effect) predominates.

Because the direction of landslide motion is subparallel to the Korean coast, the leading wave upon arrival to the coastline may be characterized by a trough or a high. The divide between the areas where such a leading wave was a trough or a high is ~10 km north of Yongdok (Fig. 15). The tsunami attained the Changgi Cape ~21 minutes after initiation of the landslide, although the ensuing crest of the tsunami did not reach the coastline until ~5 minutes later (Fig. 16). The outgoing tsunami high did not reach the Korean Peninsula until ~32 minutes after onset of the landslide (Fig. 16). The synthetic wave gages located in Deokcheon-ri and Pohang (see Fig. 3 for location) respectively record the outgoing tsunami wave high and the back-going tsunami trough as a first arrival, with significantly higher amplitude than in the previous case. The leading tsunami wave arrives 35 minutes after onset of the landslide at Deokcheon-ri and 38.5 minutes after onset of the landslide in Pohang (Fig. 17). At Deokcheon-ri the first arrival wave was the highest with an elevation of 2 m and characterized by an initial high. Subsequent waves arrived periodically at 6 minutes intervals with a wave amplitude of ~0.5 m at this location (Fig. 17). At Pohang the wave amplitude was half that at Deokcheon-ri showing again that Yongil Bay was largely sheltered from the tsunami by the Changgi Cape (Fig. 17). In this case the leading wave was the back-going tsunami trough.

The maximum tsunami elevation shows values exceeding 1 m in most of the simulation domain (Fig. 18; notice the artefacts on the NE side of the image corresponding to tsunami reflections at the edge of the simulation domain), while approaching the Korean Peninsula tsunami elevation values exceed 2 m. The color palette on Figure 18 is saturated on 3 m, so nearshore tsunami elevations are better depicted in Figure 19. Notice that tsunami elevations on the East coast of the Changgi Cape, may reach more than 9 m. It is also clear from Figures 18 and 19 that the Hupo Bank acted to focus tsunami energy on the stretch of

https://doi.org/10.1007/s12303-018-0044-x

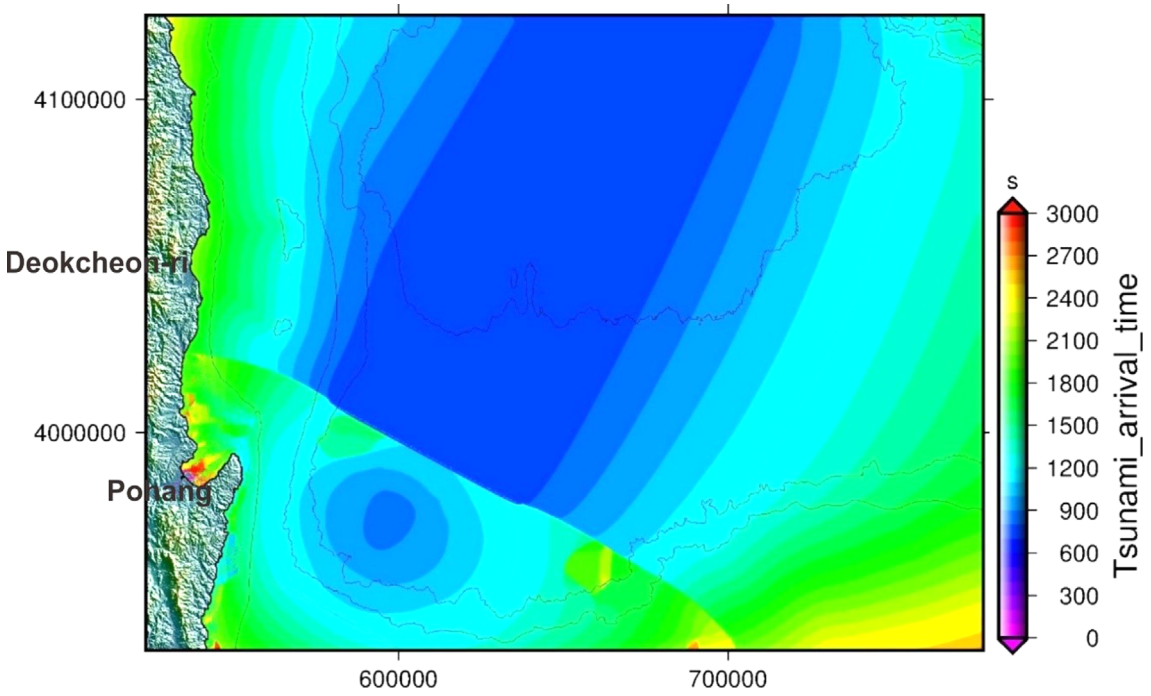

Fig. 16. Color image of time of tsunami arrival in seconds for the underwater landslide in Case 3. North is oriented up. Simulated on a 80 m grid. Tsunami color scale is in meters. Background black lines show bathymetric contours (with the 100, 500, 1000 and 2000 m iso-contours).

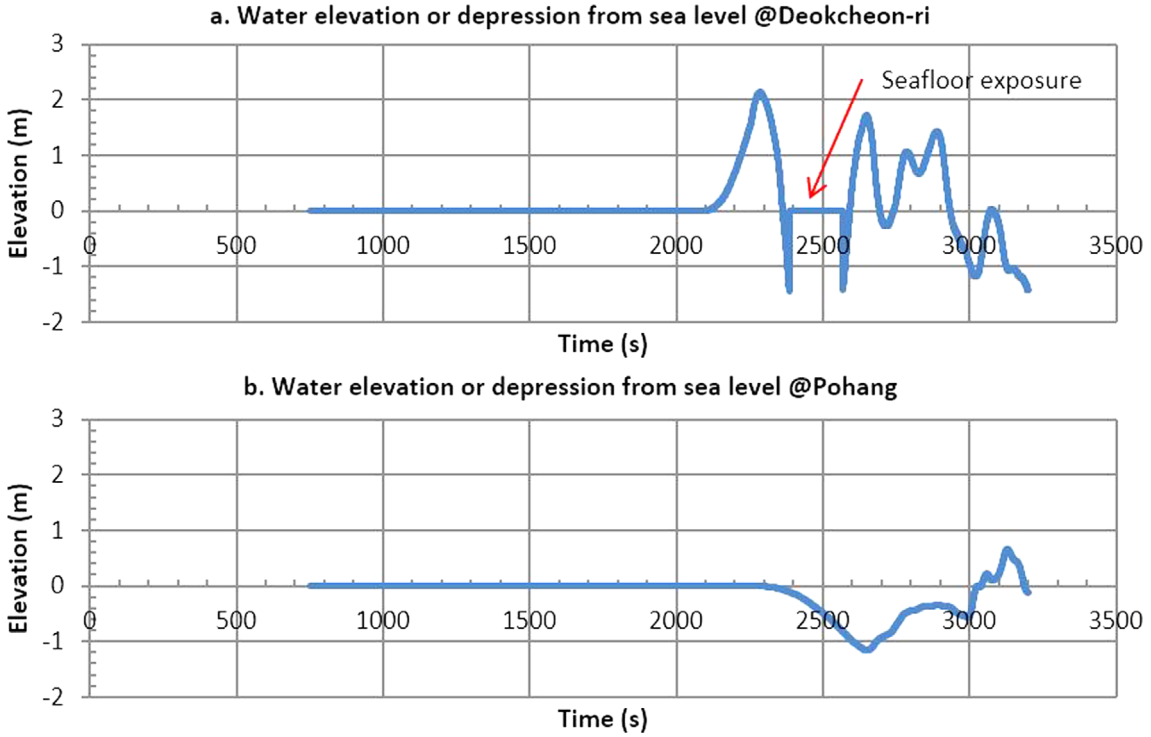

Fig. 17. Time series of tsunami elevation at the Deokcheon-ri (a) and Pohang (b) numerical wave gauges set in 1.5 and 15.8 meters water depth respectively. See Figure 3 for location of numerical wave gauges.

coast from 10 km north of Yongdok to Pyonghae. Again Pohang and the Yongil Bay in general were sheltered from the tsunami by the Changgi Cape (Figs. 18 and 19). Notice that tsunami runups on land estimated using the empirical formulation of Synolakis (1987) may reach values up to 20 m for a beach sloping 1°, which reduce to 11 m for a beach sloping 3°.

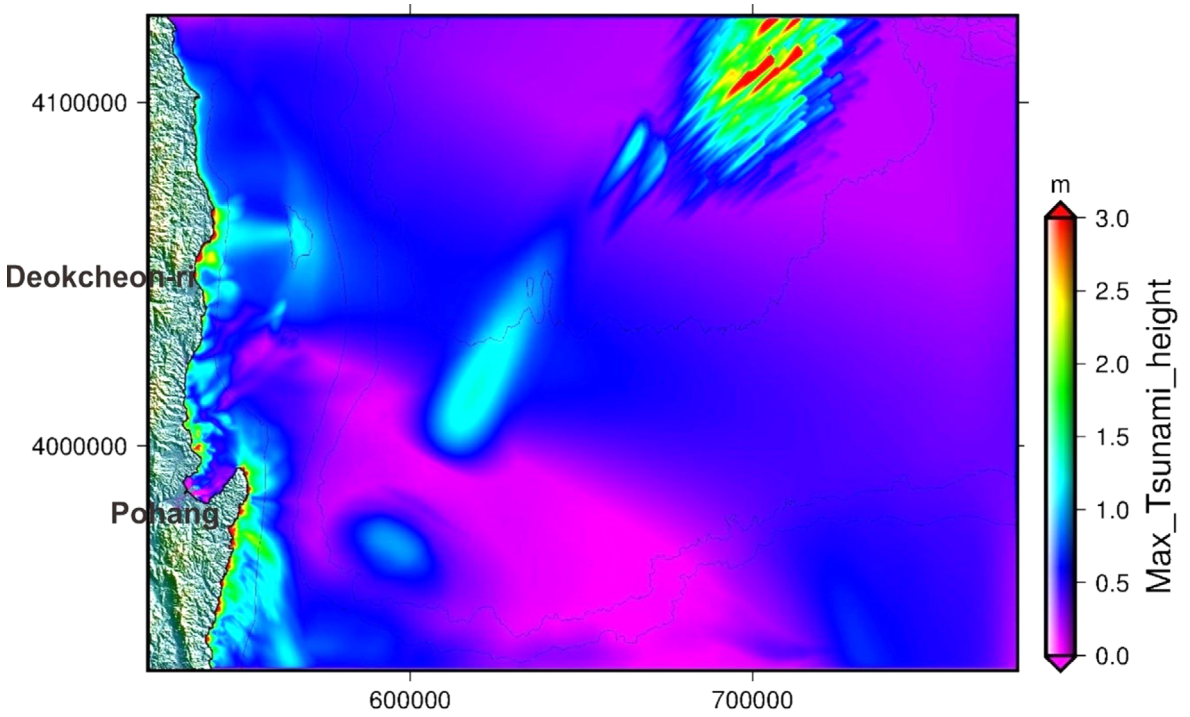

Fig. 18. Color image of maximum elevation in meters above sea level at any time during the numerical simulation for the underwater landslide in Case 3. North is oriented up. Simulated on a 80 m grid. Tsunami color scale is in meters. Background black lines show bathymetric contours (with the 100, 500, 1000 and 2000 m iso-contours).

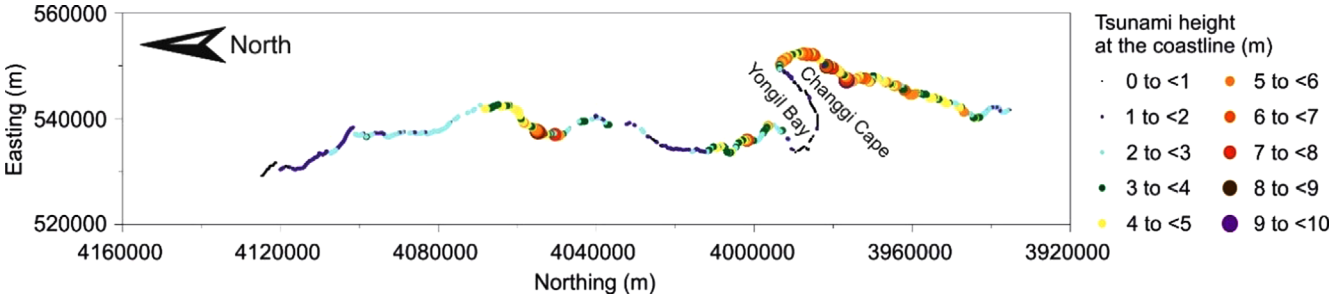

Fig. 19. Plot of maximum tsunami elevation at the coastline in meters reached during the entire tsunami simulation for the underwater landslide in Case 3. North is oriented to the left.

The tsunami arrival time of Figure 16 shows that the tsunami impacted most of the Korean Peninsula within the simulation domain ~30 minutes after onset of the landslide. These times almost doubled within the Yongil Bay. The tsunami arrival time also shows that the Hupo Bank slowed down tsunami propagation by about 2 minutes. With regard to the timing of arrival of the highest tsunami wave, Figure 20 shows that the highest waves in the stretch between Pohang and Pyonghae and also south of Kampo where reached due to reflection, refraction and diffraction from the tsunami wave at the Changgi Cape. At these locations the arrival times of the highest tsunami wave double those of the first tsunami wave (i.e., more than 50 minutes latter after onset of the landslide).

5. DISCUSSION

5.1. An Outlook at Landslide Tsunami Hazard to the Korean Coast of the East Sea

Harbitz et al. (2014) point out that the probability of a tsunami exceeding a certain value is often dominated by one (risk-driving) event. Hence, in many instances it is still efficient to use a scenario-based tsunami hazard assessment (SBTHA) such as the one proposed in this study. Where high-quality information on the spatial, size, age and other relevant characteristics of submarine landslides is not available, the simpler SBTHA approach is likely to give at least viable results for first approximation if

https://doi.org/10.1007/s12303-018-0044-x

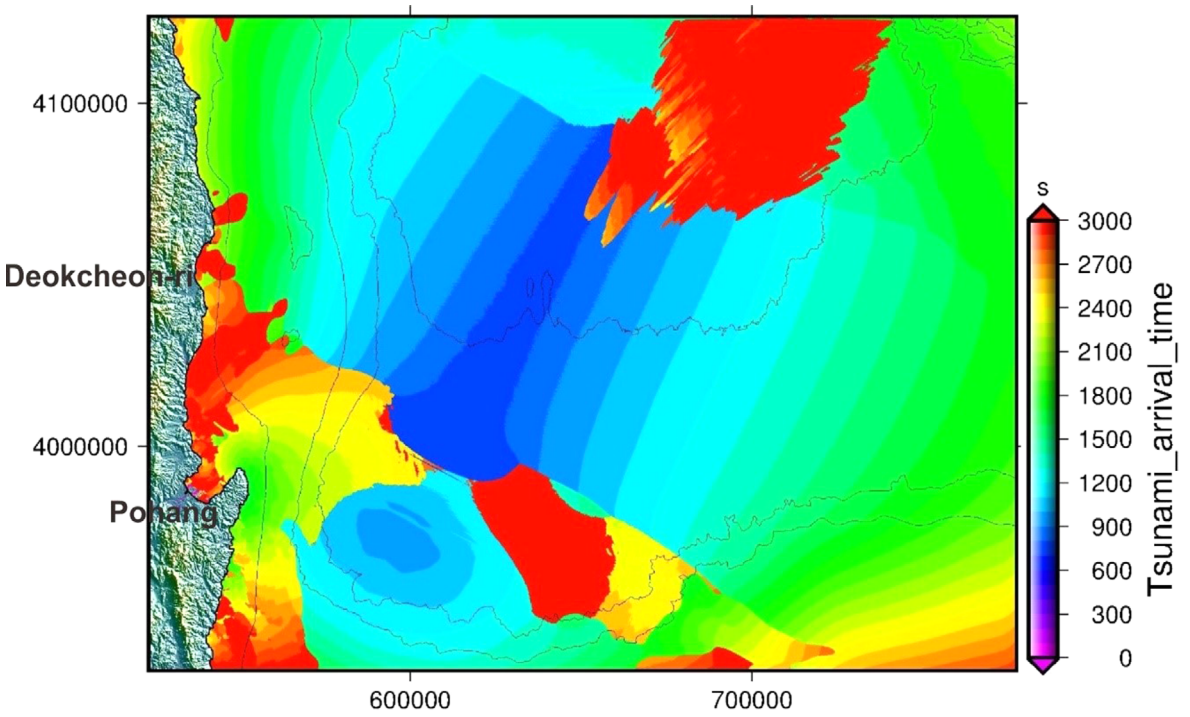

Fig. 20. Color image showing timing of arrival in seconds of maximum tsunami wave amplitude for the underwater landslide in Case 3. North is oriented up. Simulated on a 80 m grid. Tsunami color scale is in meters. Background black lines show bathymetric contours (with the 100, 500, 1000 and 2000 m iso-contours).

imperfection and uncertainty in the assumed scenario are properly acknowledged. Such imperfection and uncertainty for SBTHA of this study include the assumptions of a single stage slide and present-day sea level. It is also cautioned that the results of SBTHA only account for three examples of the many submarine landslides in the Ulleung Basin.

To understand the hazard from tsunamis it is useful to establish a tsunami wave height threshold for potential damage. Wave height or amplitude differs from runup height, which determines inundation extent. In this work no runups have been determined through modeling and just an approximation is given based on empirical formulas from Synolakis (1987). Abe (1995) indicates that the runup is approximately double the wave height or equivalent to the peak-to-trough amplitude. Based on historical Pacific tsunamis, damage to boats, docks, and swimmers may occur due to strong currents for a 0.5 m minimum tsunami amplitude or runup; more severe damage and inundation is likely at a 1.5–2 m minimum (Whitmore et al., 2008). Leonard et al. (2014) choose a tsunami runup threshold of 1.5 m (equivalent to 1.5 m peak-to-trough amplitude or *0.75 m wave height) for potential coastal damage and a 3 m runup threshold as having significant damage potential, i.e., major damage expected that may be geographically extensive.

The simulation carried out in Case 1 indicates potential coastal damage hazard zones with very local waves < 2 m high in the East Sea Korean coast between Sokcho and Yongdok (Figs. 4 and 9). These local waves could result from mid-sized landslides, not exceeding 3 km^3 in relatively gentle slopes. South of the Changgi Cape there are also potential coastal hazard zones resulting from landslides not exceeding 2 km^3 in steeper slopes of up to 6°. These landslides would induce waves that can locally attain 3 m (Figs. 5 and 13). Locations facing the Hupo Bank are at increased risk from these tsunamis as the bank seems to focus tsunami energy at certain spots along the coastline. These two sources of local landslide tsunamis (we have just investigated a couple, but there seem to be multiple past sources and there is a risk for future ones) may represent potential coastal damage along 2–3 coastal sectors that individually do not exceed 10–15 km during a particular event (Figs. 9 and 13). Time available for early warning since onset of the event is between 15–30 minutes for events originating north and along the Hupo Bank (Figs. 7 and 10) and 15 minutes maximum for events originating south of it (Figs. 11 and 14), given the narrow continental shelf and the short distance between the sources and the impact areas.

The continental margin south of the Ulleung Basin is perhaps an area where landslide tsunamis of a more regional nature, bearing more significant hazard potential, could originate. New landslides of size similar to those that have occurred in the Late Pleistocene–Holocene, which are at least one order of magnitude larger than those occurring on the continental margin to the

west of the Ulleung Basin, could produce tsunami waves > 3 m in the stretch of coastline from Ulsan in the south to Uljin in the north (Figs. 18 and 19). The timing available for early warning from landslide tsunamis originating in this area is 15–30 minutes along the affected section of the shoreline. Such a short time (despite distance) to the north of the Changgi Cape results from the particular configuration of the tsunami with respect to the coastline, which makes that the first wave to arrive in this sector is the outgoing tsunami high, not the trough (Figs. 16 and 20). The Yongil Bay seems to be a particularly well-sheltered area with respect to all tsunami sources investigated (Figs. 9, 13, 18, and 19).

5.2. Tsunami Hazard for the Korean Coast of the East Sea: Directions Forward

A major advantage of PTHA is that such analysis provides a probabilistic representation of the hazard with large epistemic (knowledge based) uncertainties related to location, release mechanisms, evolution, and return periods of the scenarios (Harbitz et al., 2014). However, for such analysis high-quality information on the spatial, size, age and other relevant characteristics of submarine landslides is needed. The risk in the PTHA analysis is to underestimate the aleatory (random) uncertainties, which would cause either underestimated PTHA results due to unrealistic assessment of uncertainties, or very high hazard levels driven essentially by large uncertainties (Harbitz et al., 2014).

Probabilistic tsunami hazard assessments (PTHAs) has largely focused on tsunamis generated by earthquakes (e.g., Choi et al., 2005; Annaka et al., 2007; Burbidge et al., 2009; Grezio et al., 2010; Sørensen et al., 2012). It is only recently that other sources, such as landslides, have started to be seriously considered (Grilli et al., 2009; Geist and Lynett, 2014; ten Brink et al., 2014). This omission has often resulted from lack of knowledge: Subduction faults are generally well known and mapped and there are a limited number of scenarios that cover the majority of the earthquake based sources (Lane et al., 2016). By comparison, there are many more landslide sources that may affect a region because landslide-generated tsunamis are by nature local features.

A conscious tsunami hazard assessment based on geological evidence would be desirable for the Korean coast of the East Sea, given the widespread evidence of large pre-historical submarine slope failures. As remembered by Geist and ten Brink (2012), although probability is key to assess tsunami hazard, a probabilistic assessment is only as good as the underlying data and assumptions. Therefore, it is critical to address the state of knowledge and the kinds of new data that would need to be collected to improve our ability to estimate probability of occurrence and tsunami hazard.

Despite submarine landslides and mass-wasting phenomena have been the subject of several studies in the Ulleung Basin of the East Sea (e.g., Lee and Chough, 2001; Lee et al., 2010, 2013; Cukur et al., 2016; Horozal et al., 2016), no systematic mapping and dating of such features has been performed. Undertaking such a task is necessary if one wants to understand the source areas, recurrence periods and approximate to some extent the dynamics of submarine landslides. The USGS has done research to identify and date significant submarine landslides along the eastern Atlantic margin of the U.S. and the Gulf of Mexico (ten Brink et al., 2006, 2009; Geist and Parsons, 2010; Geist et al., 2013) and similar approaches are being carried out in other areas such as the Mediterranean Sea (Urgeles and Camerlenghi, 2013). Recent efforts have focused on how submarine landslide probability might be determined using available geological and geophysical information and identifying the challenges of incorporating this information into PTHA (Grilli et al., 2009; Geist and Lynett, 2014; Lane et al., 2016; Pampell-Manis et al., 2016; Løvholt and Urgeles, 2017). The task calls for the acquisition of multibeam bathymetry (with collocated backscatter) to define the geometry and areal extent of submarine landslide failure areas and deposits as well as coring and chirp high resolution seismic profiling to assess the age of these events from sediment samples and correlating these ages through seismic sections. Support to drilling and coring initiatives in the East Sea should be beneficial to this end.

6. CONCLUSIONS

Submarine landslides of the western and southern margin of the Ulleung Basin have disparate characteristics, with those on the western margin having volumes of a few km^3 and limited runout. On the southern slope submarine landslides are one order of magnitude larger and may travel distances of several tens of kms. Some of these failures occur on relatively steep slopes (western margin) while others display a retrogressive behavior. All of these characteristics modify the resulting tsunamigenic potential.

Tsunami simulations from past landslides along the western and southern slopes of the Ulleung Basin provide a crude estimate of the consequences should one of these events occur at Present. The simulations show that small landslides with volumes up to 3 km^3, such as the ones present on the western slope of the Ulleung Basin may involve limited coastal damage (runup rarely exceeding 3 m) along stretches of coastline not exceeding 15 km. Where the continental shelf is relatively narrow (south of the Changgi Cape) the time available to produce early warning for such events is very limited. The larger landslides that have been mapped along the southern slopes of

https://doi.org/10.1007/s12303-018-0044-x

the Ulleung Basin involve potentially larger tsunami hazard with tsunami waves producing significant damage (runup > 3 m) along large stretches of coastline (> 50 km). Morphologic features such as the Hupo Bank help focus tsunami energy on particular coastal areas, while the Yongil bay seems largely sheltered from such events.

Several approaches to assess tsunami hazard of different methodological complexity are possible. The detailed extent, characteristics and recurrence information for submarine landslides is however uncertain or altogether lacking in Korea resulting in high uncertainty in the source term for probabilistic analysis. As a result, the risk from tsunamis is not well characterized and calls for additional data collection and further studies.

ACKNOWLEDGMENTS

This research is a contribution to KIGAM's projects "Development of Integrated Geological Information Based on Digital Mapping" (GP2017-021) and "Evaluation of seismic active faults and possibility of submarine earthquakes in the southern part of the East Sea, Korea" (NP2018-18). The Spanish "Ministerio de Economia y Competitividad" and the European Regional Development Fund through grant CTM2015-70155-R (project INSIGHT) are also acknowledged. This study is also supported by research fund of Chungnam National University and KIOST Basic Project (PE99646).

REFERENCES

Abe, K., 1995, Estimate of tsunami run-up heights from earthquake magnitudes. In: Tsuchiya, Y. and Shuto, N. (eds.), Tsunami: Progress in Prediction, Disaster Prevention and Warning, Advances in Natural and Technological Hazards Research. Springer Netherlands, p. 21–35.

Annaka, T., Satake, K., Sakakiyama, T., Yanagisawa, K., and Shuto, N., 2007, Logic-tree approach for probabilistic tsunami hazard analysis and its applications to the Japanese coasts. In: Satake, K., Okal, E.A., and Borrero, J.C. (eds.), Tsunami and Its Hazards in the Indian and Pacific Oceans, Pageoph Topical Volumes. Birkhäuser Basel, p. 577–592.

Assier-Rzadkieaicz, S., Heinrich, P., Sabatier, P.C., Savoye, B., and Bourillet, J.F., 2000, Numerical modelling of a landslide-generated tsunami: the 1979 Nice event. Pure and Applied Geophysics, 157, 1707–1727.

Bondevik, S., Løvholt, F., Harbitz, C., Mangerud, J., Dawson, A., and Inge Svendsen, J., 2005, The Storegga Slide tsunami – comparing field observations with numerical simulations. Marine and Petroleum Geology, 22, 195–208.

Brune, S., Ladage, S., Babeyko, A.Y., Müller, C., Kopp, H., and Sobolev, S.V., 2010, Submarine landslides at the eastern Sunda margin: observations and tsunami impact assessment. Natural Hazards, 54, 547–562.

Burbidge, D., Cummins, P.R., Mleczko, R., and Thio, H.K., 2009, A probabilistic tsunami hazard assessment for western Australia. In: Cummins, P.R., Satake, K., and Kong, L.S.L. (eds.), Tsunami Science Four Years after the 2004 Indian Ocean Tsunami, Pageoph Topical Volumes. Birkhäuser Basel, p. 2059–2088.

Chaytor, J.D., ten Brink, U.S., Solow, A.R., and Andrews, B.D., 2009, Size distribution of submarine landslides along the U.S. Atlantic margin. Marine Geology, 264, 16–27.

Chen, Q., Kirby, J.T., Dalrymple, R.A., Kennedy, A.B., and Chawla, A., 2000, Boussinesq modeling of wave transformation, breaking, and runup II: 2D. Journal of Waterway, Port, Coastal, and Ocean Engineering, 126, 48–56.

Choi, B.-H., Cho, Y.-S., and Yoon, S.B., 2016, Tsunami research in Korea. Natural Hazards, 84, 437–454.

Choi, B.H., Pelinovsky, E., Lee, H.J., and Woo, S.B., 2005, Estimates of tsunami risk zones on the coasts adjacent to the East (Japan) Sea based on the synthetic catalogue. Natural Hazards, 36, 355–381.

Cukur, D., Kim, S.-P., Kong, G.-S., Bahk, J.-J., Horozal, S., Um, I.-K., Lee, G.-S., Chang, T.-S., Ha, H.-J., Völker, D., and Kim, J.-K., 2016, Geophysical evidence and inferred triggering factors of submarine landslides on the western continental margin of the Ulleung Basin, East Sea. Geo-Marine Letters, 36, 425–444.

de Blasio, F.V., 2011, Introduction to the Physics of Landslides. Springer Netherlands, Dordrecht, 408 p. https://doi.org/10.1007/978-94-007-1122-8

Enet, F. and Grilli, S.T., 2007, Experimental study of tsunami generation by three-dimensional rigid underwater landslides. Journal of Waterway, Port, Coastal, and Ocean Engineering, 133, 442–454.

Fine, I.V., Rabinovich, A.B., Bornhold, B.D., Thomson, R.E., and Kulikov, E.A., 2005, The Grand Banks landslide-generated tsunami of November 18, 1929: preliminary analysis and numerical modeling. Marine Geology, 215, 45–57.

Fine, I.V., Rabinovich, A.B., Thomson, R.E., and Kulikov, E.A., 2003, Numerical modeling of tsunami generation by submarine and subaerial landslides. In: Yalçıner, A.C., Pelinovsky, E., Okal, E.A., and Synolakis, C.E. (eds.), Submarine Landslides and Tsunamis, NATO Science Series. Kluwer Academic Publishers, Dordrecht, p. 69–88.

Fryer, G.J., Watts, P., and Pratson, L.F., 2004, Source of the great tsunami of 1 April 1946: a landslide in the upper Aleutian forearc. Marine Geology, 203, 201–218.

Geist, E. and Lynett, P., 2014, Source processes for the probabilistic assessment of tsunami hazards. Oceanography, 27, 86–93.

Geist, E.L., Chaytor, J.D., Parsons, T., and ten Brink, U., 2013, Estimation of submarine mass failure probability from a sequence of deposits with age dates. Geosphere, 9, 287–298.

Geist, E.L. and Parsons, T., 2010, Estimating the epirical probability of submarine landslide occurrence. In: Mosher, D.C., Shipp, R.C., Moscardelli, L., Chaytor, J.D., Baxter, C.D.P., Lee, H.J., and Urgeles, R. (eds.), Submarine Mass Movements and Their Consequences, Advances in Natural and Technological Hazards Research. Springer Netherlands, p. 377–386.

Geist, E.L. and ten Brink, U.S., 2012, NRC/USGS Workshop Report: Landslide tsunami probability. USGS administrative report to the

US Nuclear Regulatory Commission, 43 p.

Grezio, A., Marzocchi, W., Sandri, L., and Gasparini, P., 2010, A Bayesian procedure for probabilistic tsunami hazard assessment. Natural Hazards, 53, 159–174.

Grilli, S.T. and Watts, P., 1999, Modeling of waves generated by a moving submerged body. Applications to underwater landslides. Engineering Analysis with Boundary Elements, 23, 645–656.

Grilli, S.T. and Watts, P., 2005, Tsunami generation by submarine mass failure. I: Modeling, experimental validation, and sensitivity analyses. Journal of Waterway, Port, Coastal, and Ocean Engineering, 131, 283–297.

Grilli, S.T., Vogelmann, S., and Watts, P., 2002, Development of a 3D numerical wave tank for modeling tsunami generation by underwater landslides. Engineering Analysis with Boundary Elements, 26, 301–313.

Grilli, S.T., Taylor, O.-D.S., Baxter, C.D.P., and Maretzki, S., 2009, A probabilistic approach for determining submarine landslide tsunami hazard along the upper east coast of the United States. Marine Geology, 264, 74–97.

Gusiakov, V.K., 2003, Identification of slide-generated tsunamis in the historical catalogues. In: Yalçıner, A.C., Pelinovsky, E., Okal, E.A., and Synolakis, C.E. (eds.), Submarine Landslides and Tsunamis, NATO Science Series. Kluwer Academic Publishers, Dordrecht, p. 17–24.

Harbitz, C.B., Løvholt, F., and Bungum, H., 2014, Submarine landslide tsunamis: how extreme and how likely? Natural Hazards, 72, 1341–1374.

Harbitz, C.B., Lovholt, F., Pedersen, G., and Masson, D.G., 2006, Mechanisms of tsunami generation by submarine landslides: a short review. Norsk Geologisk Tidsskrift, 86, 255.

Horozal, S., Bahk, J.J., Lee, S.H., Urgeles, R., Kim, S.P., Kim, G.Y., Cukur, D., Lee, G.H., Ryu, B.J., and Kim, J.H., 2016, Late Neogene–Quaternary submarine mass wasting along the margins of the Ulleung Basin, East Sea: geomorphologic controls and geohazard potential. Quaternary International, 392, 69–98.

Kennedy, A.B., Chen, Q., Kirby, J.T., and Dalrymple, R.A., 2000, Boussinesq modeling of wave transformation, breaking, and runup I: 1D. Journal of Waterway, Port, Coastal, and Ocean Engineering, 126, 39–47.

Lane, E.M., Mountjoy, J.J., Power, W.L., and Popinet, S., 2016, Initialising landslide-generated tsunamis for probabilistic tsunami hazard assessment in Cook Strait. International Journal of Ocean and Climate Systems, 7, 4–13.

Lee, S.H., Jung, W.-Y., Bahk, J.J., Gardner, J.M., Kim, J.K., and Lee, S.H., 2013, Depositional features of co-genetic turbidite-debrite beds and possible mechanisms for their formation in distal lobated bodies beyond the base-of-slope, Ulleung Basin, East Sea (Japan Sea). Marine Geology, 346, 124–140.

Lee, S.H., Bahk, J.-J., Kim, H.J., Kim, G.-Y., Kim, S.-P., Jeong, S.-W., and Park, S.-S., 2014, Contrasting development of the latest Quaternary slope failures and mass-transport deposits in the Ulleung Basin, East Sea (Japan Sea). In: Krastel, S., Behrmann, J.-H., Völker, D., Stipp, M., Berndt, C., Urgeles, R., Chaytor, J., Huhn, K., Strasser, M., and Harbitz, C.B. (eds.), Submarine Mass Movements and Their Consequences, Advances in Natural and Technological Hazards Research. Springer International Publishing, p. 403–412.

Lee, S.H., Bahk, J.J., Kim, H.J., Lee, K.E., Jou, H.T., and Suk, B.C., 2010, Changes in the frequency, scale, and failing areas of latest Quaternary (< 29.4 cal. ka B.P.) slope failures along the SW Ulleung Basin, East Sea (Japan Sea), inferred from depositional characters of densely dated turbidite successions. Geo-Marine Letters, 30, 133–142.

Lee, S.H. and Chough, S.K., 2001, High-resolution (2–7 kHz) acoustic and geometric characters of submarine creep deposits in the South Korea Plateau, East Sea. Sedimentology, 48, 629–644.

Lee, S.H., Chough, S.K., Back, G.G., Kim, Y.B., and Sung, B.S., 1999, Gradual downslope change in high-resolution acoustic characters and geometry of large-scale submarine debris lobes in Ulleung Basin, East Sea (Sea of Japan), Korea. Geo-Marine Letters, 19, 254–261.

Leonard, L.J., Rogers, G.C., and Mazzotti, S., 2014, Tsunami hazard assessment of Canada. Natural Hazards, 70, 237–274.

Lim, C.H., Bae, J.S., Lee, J.I., and Yoon, S.B., 2008, Propagation characteristics of historical tsunamis that attacked the east coast of Korea. Natural Hazards, 47, 95–118.

Løvholt, F., Pedersen, G., Harbitz, C.B., Glimsdal, S., and Kim, J., 2015, On the characteristics of landslide tsunamis. Philosophical Transactions of the Royal Society A, 373, 20140376. https://doi.org/10.1098/rsta.2014.0376

Løvholt, F. and Urgeles, R., 2017, Towards a probabilistic tsunami hazard analysis for the Gulf of Cadiz. Proceedings of the European Geosciences Union General Assembly 2017, Vienna, Apr. 8–13, p. EGU2017-3657-1.

Luis, J.F., 2007, Mirone: a multi-purpose tool for exploring grid data. Computers and Geosciences, 33, 31–41.

Mofjeld, H.O., González, F.I., Titov, V.V., Venturato, A.J., and Newman, J.C., 2007, Effects of tides on maximum tsunami wave heights: probability distributions. Journal of Atmospheric and Oceanic Technology, 24, 117–123.

Morgan, J.K., Silver, E., Camerlenghi, A., Dugan, B., Kirby, S., Shipp, C., and Suyehiro, K., 2009, Addressing geohazards through ocean drilling. Scientific Drilling, 7, 15–30.

Mori, N., Takahashi, T., Yasuda, T., and Yanagisawa, H., 2011, Survey of 2011 Tohoku earthquake tsunami inundation and run-up. Geophysical Research Letters, 38, L00G14. https://doi.org/10.1029/2011GL049210

Murty, T.S., 1977, Seismic Sea Waves: Tsunamis. Bulletin of the Fisheries Research Board of Canada, No. 198, 337 p.

Nicholson, T.J., Reed, W., and Cook, C., 2013, Summary of significant observations, insights, and identified opportunities for collaboration on PFHA. Proceedings of the Workshop on Probabilistic Flood Hazard Assessment (PFHA), United States Nuclear Regulatory Commission, Rockville, Jan. 29–31, pp. 10-2–10-14. https://www.nrc.gov/docs/ML1327/ML13277A074.pdf

Pampell-Manis, A., Horrillo, J., Shigihara, Y., and Parambath, L., 2016, Probabilistic assessment of landslide tsunami hazard for the northern Gulf of Mexico. Journal of Geophysical Research Oceans, 121, 1009–1027.

Papadopoulos, G.A., Gràcia, E., Urgeles, R., Sallares, V., De Martini, P.M., Pantosti, D., González, M., Yalciner, A.C., Mascle, J., Sakellar-

iou, D., Salamon, A., Tinti, S., Karastathis, V., Fokaefs, A., Camerlenghi, A., Novikova, T., and Papageorgiou, A., 2014, Historical and pre-historical tsunamis in the Mediterranean and its connected seas: geological signatures, generation mechanisms and coastal impacts. Marine Geology, 354, 81–109.

Ruffman, A., 1997, Tsunami runup mapping as an emergency preparedness planning tool: the 1929 tsunami in St. Lawrence, Newfoundland – volume 1. Emergency Preparedness Canada, Ottawa, 111 p.

Satake, K. and Tanioka, Y., 2003, The July 1998 Papua New Guinea Earthquake: mechanism and quantification of unusual tsunami generation. Pure and Applied Geophysics, 160, 2087–2118.

Satake, K. and Atwater, B.F., 2007, Long-term perspectives on giant earthquakes and tsunamis at subduction zones. Annual Review of Earth and Planetary Sciences, 35, 349–374.

Solheim, A., Berg, K., Forsberg, C.F., and Bryn, P., 2005, The Storegga Slide complex: repetitive large scale sliding with similar cause and development. Marine and Petroleum Geology, 22, 97–107.

Sørensen, M.B., Spada, M., Babeyko, A., Wiemer, S., and Grünthal, G., 2012, Probabilistic tsunami hazard in the Mediterranean Sea. Journal of Geophysical Research Solid Earth, 117, B01305. https://doi.org/10.1029/2010JB008169

Synolakis, C.E., 1987, The runup of solitary waves. Journal of Fluid Mechanics, 185, 523–545.

Tappin, D.R., Grilli, S.T., Harris, J.C., Geller, R.J., Masterlark, T., Kirby, J.T., Shi, F., Ma, G., Thingbaijam, K.K.S., and Mai, P.M., 2014, Did a submarine landslide contribute to the 2011 Tohoku tsunami? Marine Geology, 357, 344–361.

Tappin, D.R., Watts, P., and Grilli, S.T., 2008, The Papua New Guinea tsunami of 17 July 1998: anatomy of a catastrophic event. Natural Hazards and Earth System Sciences, 8, 243–266.

Tappin, D.R., 2017, Tsunamis from submarine landslides. Geology Today, 33, 190–200.

ten Brink, U.S., Barkan, R., Andrews, B.D., and Chaytor, J.D., 2009, Size distributions and failure initiation of submarine and subaerial landslides. Earth and Planetary Science Letters, 287, 31–42.

ten Brink, U.S., Chaytor, J.D., Geist, E.L., Brothers, D.S., and Andrews, B.D., 2014, Assessment of tsunami hazard to the U.S. Atlantic margin. Marine Geology, 353, 31–54.

ten Brink, U.S., Geist, E.L., and Andrews, B.D., 2006, Size distribution of submarine landslides and its implication to tsunami hazard in Puerto Rico. Geophysical Research Letters, 33. https://doi.org/10.1029/2006GL026125

Tinti, S., 2003, Needs and perspectives of tsunami research in Europe. In: Yalçıner, A.C., Pelinovsky, E., Okal, E.A., and Synolakis, C.E. (eds.), Submarine Landslides and Tsunamis, NATO Science Series. Kluwer Academic Publishers, Dordrecht, p. 9–16.

Tinti, S. and Bortolucci, E., 2000, Energy of water waves induced by submarine landslides. Pure and Applied Geophysics, 157, 281–318.

Titov, V., Rabinovich, A.B., Mofjeld, H.O., Thomson, R.E., and González, F.I., 2005, The global reach of the 26 December 2004 Sumatra tsunami. Science, 309, 2045–2048.

Urgeles, R. and Camerlenghi, A., 2013, Submarine landslides of the Mediterranean Sea: trigger mechanisms, dynamics, and frequency-magnitude distribution. Journal of Geophysical Research Earth Surface, 118, 2013JF002720. https://doi.org/10.1002/2013JF002720

Ward, S.N., 2001, Landslide tsunami. Journal of Geophysical Research Solid Earth, 106, 11201. https://doi.org/10.1029/2000JB900450

Watts, P., 1998, Wavemaker curves for tsunamis generated by underwater landslides. Journal of Waterway Port Coastal and Ocean Engineering, 124, 127–137.

Watts, P., Grilli, S.T., Kirby, J.T., Fryer, G.J., and Tappin, D.R., 2003, Landslide tsunami case studies using a Boussinesq model and a fully nonlinear tsunami generation model. Natural Hazards and Earth System Sciences, 3, 391–402.

Watts, P., Grilli, S.T., Tappin, D.R., and Fryer, G.J., 2005, Tsunami generation by submarine mass failure. II: Predictive equations and case studies. Journal of Waterway, Port, Coastal, and Ocean Engineering, 131, 298–310.

Watts, P., Imamura, F., and Grilli, S., 2000, Comparing model simulations of three benchmark tsunami generation cases. Science of Tsunami Hazards, 18, 107–124.

Waythomas, C.F., Watts, P., Shi, F., and Kirby, J.T., 2009, Pacific Basin tsunami hazards associated with mass flows in the Aleutian arc of Alaska. Quaternary Science Reviews, 28, 1006–1019.

Wei, G. and Kirby, J.T., 1995, Time-dependent numerical code for extended Boussinesq Equations. Journal of Waterway, Port, Coastal, and Ocean Engineering, 121, 251–261.

Wei, G., Kirby, J.T., and Sinha, A., 1999, Generation of waves in Boussinesq models using a source function method. Coastal Engineering, 36, 271–299.

Wessel, P., Smith, W.H.F., Scharroo, R., Luis, J., and Wobbe, F., 2013, Generic mapping tools: improved version released. Eos Transactions American Geophysical Union, 94, 409–410.

Whitmore, P., Benz, H., Bolton, M., Crawford, G., Dengler, L., Fryer, G., Goltz, J., Hansen, R., Kryzanowski, K., Malone, S., Oppenheimer, D., Petty, E., Rogers, G., and Wilson, J., 2008, NOAA/West Coast and Alaska Tsunami Warning Center Pacific Ocean response criteria. Science of Tsunami Hazards, 27, 1–19.

Xiao, L., Ward, S.N., and Wang, J., 2015, Tsunami squares approach to landslide-generated waves: application to Gongjiafang Landslide, Three Gorges Reservoir, China. Pure and Applied Geophysics, 172, 3639–3654.